

# Characterization of Dark-Matter-induced anisotropies in the diffuse gamma-ray background

Mattia Fornasa<sup>1,2,3</sup>, Jesús Zavala<sup>4,5,6</sup>, Miguel A. Sánchez-Conde<sup>7</sup>,  
Jennifer M. Siegal-Gaskins<sup>8,9</sup>, Timur Delahaye<sup>10</sup>, Francisco Prada<sup>1,10,11</sup>,  
Mark Vogelsberger<sup>12</sup>, Fabio Zandanel<sup>1</sup> and Carlos S. Frenk<sup>13</sup>

<sup>1</sup> Instituto de Astrofísica de Andalucía (IAA - CSIC), Glorieta de la Astronomía, Granada, Spain

<sup>2</sup> MultiDark fellow, E-mail: [mattia.fornasa@nottingham.ac.uk](mailto:mattia.fornasa@nottingham.ac.uk)

<sup>3</sup> School of Physics and Astronomy, University of Nottingham, University Park, Nottingham, NG7 2RD, United Kingdom

<sup>4</sup> Department of Physics and Astrophysics, University of Waterloo, 200 University Avenue West, Waterloo, Canada

<sup>5</sup> Perimeter Institute for Theoretical Physics, 31 Caroline St. N., Waterloo, ON, N2L 2Y5, Canada

<sup>6</sup> CITA National Fellow, E-mail: [jzavalaf@uwaterloo.ca](mailto:jzavalaf@uwaterloo.ca)

<sup>7</sup> SLAC National Accelerator Laboratory & Kavli Institute for Particle Astrophysics and Cosmology, 2575 Sand Hill Road, Menlo Park, CA, 94025, USA

<sup>8</sup> Einstein fellow

<sup>9</sup> California Institute of Technology, Pasadena, CA 91125 USA

<sup>10</sup> Instituto de Física Teórica UAM/CSIC, Universidad Autónoma de Madrid Cantoblanco, 28049, Madrid, Spain

<sup>11</sup> Campus of International Excellence UAM/CSIC, Cantoblanco, E-28049 Madrid, Spain

<sup>12</sup> Harvard-Smithsonian Center for Astrophysics, 60 Garden St., Cambridge, MA 02138, USA

<sup>13</sup> Institute for Computational Cosmology, Dept. of Physics, University of Durham, South Road, Durham, DM1 3LE, United Kingdom

4 July 2012

## ABSTRACT

The Fermi-LAT collaboration has recently reported the detection of angular power above the photon noise level in the diffuse gamma-ray background between 1 and 50 GeV. Such signal can be used to constrain a possible contribution from Dark-Matter-induced photons. We estimate the intensity and features of the angular power spectrum (APS) of this potential Dark Matter (DM) signal, for both decaying and annihilating DM candidates, by constructing template all-sky gamma-ray maps for the emission produced in the galactic halo and its substructures, as well as in extragalactic (sub)halos. The DM distribution is given by state-of-the-art  $N$ -body simulations of cosmic structure formation, namely Millennium-II for extragalactic (sub)halos, and Aquarius for the galactic halo and its subhalos. We use a hybrid method of extrapolation to account for (sub)structures that are below the resolution limit of the simulations, allowing us to estimate the total emission all the way down to the minimal self-bound halo mass. We describe in detail the features appearing in the APS of our template maps and we estimate the effect of various uncertainties such as the value of the minimal halo mass, the fraction of substructures hosted in a halo and the shape of the DM density profile. Our results indicate that the fluctuation APS of the DM-induced emission is of the same order as the Fermi-LAT APS, suggesting that one can constrain this hypothetical emission from the comparison with the measured anisotropy. We also quantify the uncertainties affecting our results, finding “theoretical error bands” spanning more than two orders of magnitude and dominated (for a given particle physics model) by our lack of knowledge of the abundance of low-mass (sub)halos.

## 1 INTRODUCTION

The isotropic gamma-ray background (IGRB) is the radiation that remains after the resolved sources (both extended and point-like) and the galactic foreground (produced by the interaction of cosmic rays with the interstellar medium) are subtracted from the all-sky gamma-ray emission. A *guaranteed* component of the IGRB is the emission of unresolved known sources, whose contribution has been estimated from population studies of their resolved counterparts: *blazars* (Stecker et al. 1993; Stecker & Salamon 1996; Muecke & Pohl 1998; Narumoto & Totani 2006; Dermer 2007;

Pavlidou & Venters 2008; Inoue & Totani 2009; Abdo et al. 2010b; Abazajian et al. 2011; Stecker & Venters 2011; Singal et al. 2012), *star-forming galaxies* (Bhattacharya et al. 2009; Fields et al. 2010; Makiya et al. 2011; Ackermann et al. 2012b; Lacki et al. 2012; Chakraborty & Fields 2012), *radio galaxies* (Stawarz et al. 2006; Massaro & Ajello 2011; Inoue 2011), *pulsars and milli-second pulsars* (Faucher-Giguere & Loeb 2010; Siegal-Gaskins et al. 2011), *Gamma-Ray Bursts* (Casanova et al. 2008) and *Type Ia Supernovae* (Lien & Fields 2012). Additional processes may also contribute to the IGRB such as cosmological structure formation shocks

(e.g. Loeb & Waxman 2000; Gabici & Blasi 2003), and interactions of cosmic rays (CRs) with the extragalactic background light (EBL) (Kalashev et al. 2009) or with small solar system bodies (Moskalenko & Porter 2009).

Current estimates, however, suggest that the total unresolved emission from the classes listed above is not able to account for the whole IGRB intensity (e.g. Ajello 2011), which strengthens the possibility that additional, unconfirmed sources are required to match the data. Gamma rays from Dark Matter (DM) annihilation or decay could explain the missing emission.

DM is the dominant matter component of the Universe, responsible for approximately one quarter of the energy density today (e.g. Jarosik et al. 2011). We know little about its nature, apart from the fact that it has to be non baryonic. A well-studied class of DM candidates is that of Weakly Interacting Massive Particles (WIMPs), whose masses and interactions (set by the scale of weak interactions), offer promising non-gravitational signals for their detection in the near future. Within the context of annihilating DM, WIMPs are favoured by the fact that they naturally have a relic density that matches the observed DM abundance (e.g. Kolb & Turner 1994; Bertone et al. 2005), while for decaying DM, it has been shown that WIMPs can have a decay lifetime larger than the age of the Universe, and are therefore viable DM candidates (see e.g. Bolz et al. 2001; Arvanitaki et al. 2009). WIMPs are also appealing because their existence is predicted by fundamental theories beyond the Standard Model of Particle Physics, such as Supersymmetry (SUSY), Universal Extra-Dimensions or models with  $T$ -parity. In this paper we assume that DM is made of WIMPs, without making a specific assumption about the theoretical particle physics model from which WIMPs arise.

This work is concerned with *indirect detection* of DM, i.e., the possibility of revealing the presence of DM from detection of its annihilation or decay products. In particular, we focus here on the case of gamma rays as by-products, studying the possible contribution to the IGRB coming from the DM annihilations (or decays) in the smooth DM halo of the Milky Way (MW) and its galactic subhalos, as well as from extragalactic (sub)halos. These contributions have already been estimated in the past using analytical and numerical techniques (e.g. Ullio et al. 2002; Taylor & Silk 2003; Ando 2005; Ando & Komatsu 2006; Ando et al. 2007b; Siegal-Gaskins 2008; Ando 2009; Fornasa et al. 2009; Zavala et al. 2010; Ibarra et al. 2010; Hutsi et al. 2010; Cirelli et al. 2011; Zavala et al. 2011). The recent Fermi-LAT measurement of the energy spectrum of the IGRB has been used to put constraints on the nature of the DM candidate by requiring that the DM-induced emission should not exceed the observed IGRB (Abdo et al. 2010a; Hutsi et al. 2010; Zavala et al. 2011; Calore et al. 2012). The constraints derived are quite competitive: for instance, the most optimistic scenario considered by Abdo et al. (2010a) puts a strong upper limit to the annihilation cross section, which is already of the order of the thermal relic value for a DM particle lighter than 200-300 GeV.

The energy spectrum is not the only piece of information we can extract from the IGRB. Thanks to the good angular resolution of Fermi-LAT, it is also possible to measure its angular power spectrum (APS) of anisotropies. Ackermann et al. (2012a) reported a detection of angular power in the multipole range between  $\ell = 155$  and 504 with a significance that goes from  $7.2\sigma$  (in the energy bin between 2 and 5 GeV) to  $2.7\sigma$  (between 10 and 50 GeV), which represents the first detection of intrinsic anisotropies in the IGRB.

There are different predictions for the normalization and shape of the APS produced by different populations of unresolved sources, both astrophysical (Ando et al. 2007a; Ando & Pavlidou

2009; Siegal-Gaskins et al. 2011) and associated with DM (Ando 2005; Ando & Komatsu 2006; Ando et al. 2007b; Cuoco et al. 2007, 2008; Taoso et al. 2009; Siegal-Gaskins 2008; Fornasa et al. 2009; Siegal-Gaskins & Pavlidou 2009; Ando 2009; Zavala et al. 2010; Ibarra et al. 2010; Cuoco et al. 2011). The comparison of these predictions with the Fermi-LAT APS data can, in principle, constrain the contribution of each source class to the IGRB (Cuoco et al. 2012). The analysis from Ackermann et al. (2012a) seems to suggest an interpretation in terms of a single population of unresolved, unclustered objects, due to the fact that the APS is roughly scale-independent over the energy range analysed. This recent measurement can then be used to complement other constraints on a possible DM contribution to the IGRB. In the present paper, we take a first step in obtaining such constraints by revisiting and updating the prediction of the DM-induced emission (through decay and annihilation) and its associated APS, as well as estimating the uncertainties involved. The comparison of these predictions with the Fermi-LAT APS data will be done in a follow-up study.

In order to compute the DM-induced APS we combine the results of two  $N$ -body simulations of the galactic (Aquarius, hereafter AQ, Springel et al. 2008) and extragalactic (Millennium-II, hereafter MS-II, Boylan-Kolchin et al. 2009) DM structures, to construct all-sky maps of the gamma-ray emission coming from the annihilation and decay of DM in the Universe around us. Although we only focus here on the study of the anisotropy patterns in the gamma-ray emission, these maps represent *per se* a useful tool for future projects on indirect DM detection and we plan to make them available shortly after the publication of the follow-up paper dedicated to the comparison with the Fermi-LAT APS data.

The extragalactic component is expected to be almost isotropic (see, e.g., Zavala et al. 2010), while the smooth galactic one is characterized by an intrinsic anisotropy, as a consequence of our position in the MW halo. The presence of galactic subhalos, however, reduces the expected gradient of the DM-induced gamma-ray flux as one moves away from the Galactic Center (GC). In fact, due to the large abundance of substructures and their more extended distribution, strong gamma-ray emission is also expected quite far away from the GC (as it can be seen, e.g., in Springel et al. 2008; Fornasa et al. 2009; Cuesta et al. 2011; Sánchez-Conde et al. 2011).

Even though numerical simulations represent the most reliable method to model the non-linear evolution of DM, they are limited by resolution. Since the minimum self-bound mass ( $M_{\min}$ ) of DM halos is expected to be many orders of magnitude below the capabilities of current simulations<sup>1</sup>, this poses a challenge for an accurate prediction and represents one of our largest sources of uncertainty (e.g. Taylor & Silk 2003; Springel et al. 2008; Siegal-Gaskins 2008; Ando 2009; Fornasa et al. 2009; Zavala et al. 2010; Kamionkowski et al. 2010; Sánchez-Conde et al. 2011; Pinzke et al. 2011; Gao et al. 2011). To address this problem, we use a hybrid method that models the (sub)halo population below the mass resolution of the simulations by extrapolating the behaviour of the resolved structures in the MS-II and AQ simulations towards lower masses. Furthermore, we compute multiple sky maps with different values of  $M_{\min}$  to determine with more precision what is the impact of this parameter on the the DM-induced emission. We

<sup>1</sup> The actual value of  $M_{\min}$  is related to the nature of the DM particle, with typical values covering a quite large range, approximately between  $10^{-12} M_{\odot}$  and  $10^{-3} M_{\odot}$  (e.g. Profumo et al. 2006; Bringmann 2009).

also consider possible effects due to different DM density profiles for the smooth halo of the MW.

Such a detailed study of the uncertainties associated with the APS allows us to quantify, in addition to the normalization and shape of the APS, a “theoretical uncertainty band”, that will prove to be useful in the comparison of our predictions with the Fermi-LAT APS data.

The paper is organized as follows. In Sec. 2 we describe the mechanisms responsible for the gamma-ray emission from DM annihilation or decay. We then present how the data from the MS-II and AQ simulations are used to construct template maps of DM-induced gamma-ray emission from extragalactic DM (sub)halos (Sec. 3) and from the smooth galactic halo and its subhalos (Sec. 4). In Sec. 5 we present the energy and angular power spectra, discussing the different components and estimating their uncertainties. We discuss the implications of our results in Sec. 6, while Sec. 7 is devoted to a summary and our conclusions.

## 2 DARK-MATTER-INDUCED GAMMA-RAY EMISSION

In the case of DM annihilation, the gamma-ray intensity (defined as the number of photons collected by a detector per unit of area, time, solid angle and energy) produced in a direction  $\Psi$  is:

$$\frac{d\Phi}{dE}(E_\gamma, \Psi) = \frac{(\sigma_{\text{ann}} v)}{8\pi m_\chi^2} \int_{\text{l.o.s.}} d\lambda \sum_i B_i \frac{dN_\gamma^i(E_\gamma(1+z))}{dE} \times \rho^2(\lambda(z), \Psi) e^{-\tau_{\text{EBL}}(z, E_\gamma)}, \quad (1)$$

where  $E_\gamma$  is the observed photon energy,  $m_\chi$  is the mass of the DM particle and  $(\sigma_{\text{ann}} v)$  its annihilation cross section. The sum runs over all annihilation channels, each one characterized by a branching ratio,  $B_i$ , and photon spectrum (yield),  $dN_\gamma^i/dE$ , computed at the energy of emission. The integration is over the line of sight (parameterized by  $\lambda$ ) to account for the redshift-dependent DM density field  $d\lambda = c dz H(z)^{-1}$ . The exponential factor accounts for photon absorption from pair production due to interactions with the EBL along the line of sight, parametrized by an optical depth  $\tau_{\text{EBL}}(z, E_\gamma)$ , which we take from the model developed in Dominguez et al. (2010)<sup>2</sup>. The first part of the integrand in Eq. 1 is usually referred to as the “particle physics factor” and only depends on the properties of DM as a particle, whereas the second part is called the “astrophysical factor” and depends on how DM is distributed in space<sup>3</sup>.

In the case of DM decay, Eq. 1 should be re-written as:

$$\frac{d\Phi}{dE}(E_\gamma, \Psi) = \frac{1}{4\pi m_\chi \tau} \int_{\text{l.o.s.}} d\lambda \sum_i B_i \frac{dN_\gamma^i(E_\gamma(1+z))}{dE} \times \rho(\lambda(z), \Psi) e^{-\tau_{\text{EBL}}(z, E_\gamma)}, \quad (2)$$

where the decay lifetime  $\tau$  is used instead of the annihilation cross section and the dependence on density is linear instead of quadratic.

In the current section we describe the particle physics factor,

introducing the mechanisms of gamma-ray production considered. Secs. 3 and 4 are devoted to the astrophysical factor.

As mentioned in the Introduction, rather than considering a specific particle physics model, we focus on a general WIMP candidate, which, for our purposes, is completely defined by  $m_\chi$ ,  $(\sigma_{\text{ann}} v)$  or  $\tau$ , and its gamma-ray photon yield. The latter receives contributions from three different mechanisms of emission:

- *Prompt emission*: This radiation comes from the products of DM annihilation/decay directly, without any interaction with external particles. Within this first category, one can distinguish three different processes: *i*) gamma-ray lines from direct annihilation/decay into photons, *ii*) hadronization of quarks followed by neutral pion decay into photons and *iii*) gamma rays from final state radiation and internal bremsstrahlung whenever there are charged final states. For DM annihilation, the branching ratios for monochromatic lines are usually subdominant and quite model-dependent (at least for SUSY models), while for DM decay, emission lines may be more prominent (Choi et al. 2010; Vertongen & Weniger 2011; Gomez-Vargas et al. 2012). In this work, we do not consider the emission from monochromatic lines, instead, we focus on mechanisms *ii*) and *iii*), which are characterized by a continuum emission (e.g. Fornengo et al. 2004; Bertone et al. 2005; Bergstrom et al. 2005; Bringmann et al. 2008). The continuum emission induced by hadronization shows some dependence on the DM mass and the particular annihilation/decay channel, but it is a mild one and the shape is more or less universal. Finally, internal bremsstrahlung may also contribute inducing harder spectra and the possibility of bumps near the energy cut-off set by  $m_\chi$  (see e.g. Bringmann et al. 2008, 2009, 2012).

- *Inverse Compton (IC) up-scattering*: This secondary radiation originates when low energy background photons are up-scattered by the leptons produced by DM annihilation/decay. Since large  $\gamma$  factors are required, usually one focuses on the case of electrons and positrons interacting with the Cosmic Microwave Background (CMB) photons and with starlight (either directly or re-scattered by dust). The amplitude of the IC emission and its energy spectrum depends on the injection spectrum of  $e^+/e^-$  and on the energy density of the background radiation fields (Colafrancesco et al. 2006; Profumo & Jeltema 2009; Zavala et al. 2011). For massive DM candidates, those IC photons can fall within the energy range detected by Fermi-LAT and, in some cases, represent a significant contribution to the DM-induced emission (Profumo & Jeltema 2009; Meade et al. 2010; Hutsi et al. 2010; Pinzke et al. 2011). See Appendix A for details on the computation of the IC emission. We note that for the case of extragalactic DM (sub)halos (Sec. 3) we only consider the CMB as a background source. This is mainly because the bulk of the emission comes from small (sub)halos (see Sec. 5.1) that are essentially empty of stars and therefore lack any starlight background (see e.g. Profumo & Jeltema 2009; Zavala et al. 2011). On the other hand, for the case of the MW smooth halo, a complete model for the MW radiation field is used (see Sec. 4.1).

- *Hadronic emission*: This radiation comes from the interaction of hadrons produced by DM annihilation/decay with the interstellar gas, and its contribution depends on the injection spectrum of hadrons and on the spatial distribution of ambient gas. To implement this component we follow the method described in Delahaye et al. (2011) (see also Cholis et al. 2011; Vladimirov et al. 2011) and present the details of the calculation

<sup>2</sup> We have not checked the effect of other EBL attenuation models, since for the energies we consider in this work (from 0.5 GeV to 50 GeV), the contribution of the damping  $e^{-\tau_{\text{EBL}}}$  factor is marginal.

<sup>3</sup> The particle physics and astrophysical factors are not completely independent from each other: the presence of  $M_{\text{min}}$ , which is fixed by the particle physics nature of the DM candidate, determines the minimum (sub)halo mass scale to be considered. Moreover, the dependence on redshift is both for the DM distribution and for the energy in the photon yield  $dN_\gamma/dE$ .

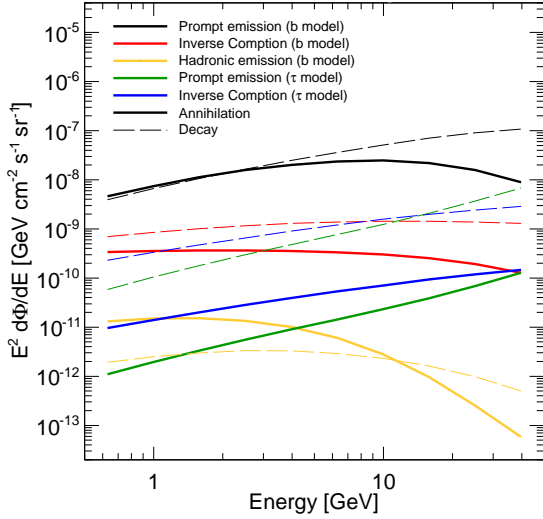


**Figure 1.** Gamma-ray intensity from DM annihilation (solid lines) and decay (dashed lines) coming from the MW smooth halo (see Sec. 4.1). For the “*b*-model” (black, red and yellow lines) the mass of the DM particle is 200 GeV for the case of annihilation and 2 TeV for decay. We assume  $(\sigma_{\text{ann}}v) = 3 \times 10^{-26} \text{ cm}^3 \text{ s}^{-1}$  and  $\tau = 2 \times 10^{27} \text{ s}$ , respectively. For the “ $\tau$ -model” (blue and green lines) the parameters are the same except for the mass which is 2 TeV for both annihilating and decaying DM. Black and blue lines indicate prompt-emission, red and green IC emission, and yellow hadronic emission. The latter is not shown for the  $\tau$ -model.

in Appendix B. We only consider this additional component for the case of the MW smooth DM halo.

As benchmarks, in the remainder of this paper, we consider two commonly-used annihilation/decay channels, with which we illustrate the role of the different mechanisms: a “*b*-model” for annihilation/decay entirely into  $b\bar{b}$  quarks ( $B_b = 1$ ) and a “ $\tau$ -model” for annihilation/decay into  $\tau^+\tau^-$  ( $B_\tau = 1$ ). The photon and  $e^+/e^-$  yields are computed using the tables presented in Cirelli et al. (2011). For both cases, we fix the annihilation cross section and decay life time to  $3 \times 10^{-26} \text{ cm}^3 \text{ s}^{-1}$  and  $2 \times 10^{27} \text{ s}$ , respectively. The DM mass is selected to be 200 GeV for the *b* channel in the case of annihilating DM and 2 TeV otherwise. These values are chosen to be slightly below the most recent exclusion limits set by the Fermi-LAT data (Ackermann et al. 2011; Dugger et al. 2010; Huang et al. 2011).

In Fig. 1 we compare the gamma-ray production mechanisms listed above. The lines indicate the energy spectrum of the emission from annihilation (solid) or decay (dashed) of DM in the MW smooth halo (see Sec. 4.1). For the *b*-model, prompt emission (black lines) always dominates over IC (red lines) and hadronic emission (yellow lines), both for annihilation and decay. On the other hand, for the  $\tau$ -model, IC (blue lines) overcomes the prompt-emission (green lines) at low energies. For the  $\tau$ -model, hadronic emission is negligible and is not plotted.

### 3 THE GAMMA-RAY EMISSION FROM EXTRAGALACTIC (SUB)HALOS

#### 3.1 Resolved (sub)halos in the Millennium-II simulation (EG-MSII)

The MS-II follows the formation and evolution of DM structures in a comoving cube of  $L = 100 \text{ Mpc}/h$  on a side and a total of  $(2160)^3$  simulation particles (Boylan-Kolchin et al. 2009). The simulation is done within the context of a WMAP1 cosmology with the following parameters:  $\Omega_m = 0.25$ ,  $\Omega_\Lambda = 0.75$ ,  $h = 0.73$ ,  $\sigma_8 = 0.9$  and  $n_s = 1$ ; where  $\Omega_m$  and  $\Omega_\Lambda$  are the contribution from matter and cosmological constant to the mass/energy density of the Universe, respectively,  $h$  is the dimensionless Hubble constant parameter at redshift zero,  $n_s$  is the spectral index of the primordial power spectrum, and  $\sigma_8$  is the rms amplitude of linear mass fluctuations in  $8 \text{ Mpc}/h$  spheres at redshift zero. Its mass resolution is  $6.89 \times 10^6 M_\odot/h$  and there are 68 snapshots recording the particle distribution at different redshifts between  $z = 127$  and  $z = 0$ .

Instead of working directly with the particles in the simulations, we use the MS-II (sub)halo catalogs, which are constructed using a friend-of-friends (FOF) algorithm (Davis et al. 1985) and the SUBFIND code (Springel et al. 2001) that identifies self-bound substructures within FOF halos. Dealing with the (sub)halo catalogs, instead of the particle data, has two advantages: it is much less expensive computationally and, more importantly, it avoids resolution effects near the centre of DM (sub)halos, where the simulation particles severely underestimate the DM density (note that this is precisely the region with the highest gamma-ray production rate). On the other hand, we are neglecting the contribution from the DM mass that does not belong to (sub)halos. The emission rate from unclustered regions, however, is likely to be negligible especially for DM annihilations (see, e.g. Angulo & White 2009 who analytically estimated that between 80-95% of the mass is in collapsed objects. In the case of decaying DM this suggests that, by neglecting unbound particles, we underestimate the luminosity by, at most, 20%).

The MS-II (sub)halo catalog contains the global properties needed for each object: its virial mass  $M_{200}$  (defined as the mass up to  $r_{200}$ , where the enclosed density is 200 times the critical density), its maximum circular velocity  $V_{\text{max}}$  and the radius  $r_{\text{max}}$  where this velocity is attained. The latter two quantities completely determine the annihilation/decay luminosity for each halo if we assume that they have a spherically symmetric density distribution given by a Navarro-Frenk-White (NFW) profile (Navarro et al. 1997). The number of gamma rays (per unit of time and energy) coming from a (sub)halo with a boundary at  $r_{200}$  is then given by  $L = f_{\text{PP}} L'$ , where:

$$f_{\text{PP}} = \frac{(\sigma_{\text{ann}}v)}{2m_\chi^2} \sum_i B_i \frac{dN_\gamma^i}{dE}, \quad (3)$$

$$L' \equiv L_{\text{ann}} = 1.23 \frac{V_{\text{max}}^4}{G^2 r_{\text{max}}} \left[ 1 - \frac{1}{(1 + c_{200})^3} \right], \quad (4)$$

for the case of annihilation, and

$$f_{\text{PP}} = \frac{1}{m_\chi \tau} \sum_i B_i \frac{dN_\gamma^i}{dE}, \quad (5)$$

$$L' \equiv L_{\text{decay}} = 2.14 \frac{V_{\text{max}}^2 r_{\text{max}}}{G} \left[ \ln(1 + c_{200}) - \frac{c_{200}}{1 + c_{200}} \right], \quad (6)$$

for the case of decay.

The concentration  $c_{200}$  is also determined from  $V_{\max}$  and  $r_{\max}$  inverting the following relation (e.g. Springel et al. 2008):

$$14.426 \left( \frac{V_{\max}}{H(z) r_{\max}} \right)^2 = \frac{200}{3} \frac{c_{200}^3}{\ln(1 + c_{200}) - c_{200}/(1 + c_{200})}. \quad (7)$$

The choice of the NFW density profile is motivated by its universality and by the fact that it gives a good fit to simulated DM (sub)halos over a large mass range. However, assuming other DM density profiles could have an impact on the total gamma-ray emission, as well as on the shape and normalization of the APS. A discussion about this possible source of uncertainty is left for Sec. 6.

We define as EG-MSII the signal coming from (sub)halos in the MS-II catalogs with at least 100 particles; below this number, the mass and abundance of DM objects in the MS-II can become unreliable. This sets an “effective” mass resolution of  $M_{\text{res}} = 6.89 \times 10^8 M_{\odot}/h$  for the extragalactic contribution. DM structures with less than a few thousand particles can be affected by numerical effects (gravitational softening and two-body relaxation, see e.g. Diemand et al. 2004) that could influence the values of  $V_{\max}$  and  $r_{\max}$  and, as a consequence,  $L_{\text{ann}}$  or  $L_{\text{decay}}$ . We implement the prescription described in Zavala et al. (2010) to correct for these effects.

In order to simulate the past light cone we need to probe a volume which is much larger than the MS-II box. To do this, we follow closely the procedure given in Zavala et al. (2010) which can be summarized as follows. The region around the observer is divided into concentric shells, each of them centered in redshift space on the discrete values  $z_i$  corresponding to each simulation output. The volume defined by each shell has a fixed size in redshift space and a corresponding comoving thickness which is filled with identical, non-overlapping copies of the MS-II box at the redshift  $z_i$  (see Fig. 9 of Zavala et al. 2010). In order to compute the DM-induced gamma-ray emission from a given direction  $\Psi$ , we follow the line of sight defined by  $\Psi$  that crosses the MS-II replicas, and sum up the emission produced in all the (sub)halos encountered. The projection into a 2-dimensional map is done with the HEALPix package<sup>4</sup> (Gorski et al. 2005), assuming  $N_{\text{side}}=512$ , corresponding to an angular area of approximately  $4 \times 10^{-6}$  sr for each pixel. If a given halo subtends an area larger than this value, then it is considered as an extended source. In this case, each of the pixels covered by the particular halo is filled with a fraction of the total halo luminosity, assuming the corresponding projected surface density profile.

To avoid the repetition of the same structures along the line of sight (which would introduce spurious periodicity along this direction), Zavala et al. (2010) used an independent random rotation and translation of the pattern of boxes that tessellates each shell. This method, however, still leaves a spurious angular correlation at a scale  $\Delta\theta$  corresponding to the comoving size of the simulation box, which mainly manifests itself as a peak in the APS centered on  $\ell^* = 2\pi/\Delta\theta$ . This angular scale decreases as we go deeper in redshift, since each copy of the MS-II cube covers smaller and smaller angles. This implies that the periodicity-induced peak will be located at a different multipole for each shell. Once the contributions from all shells are added up, this effect is largely averaged out, and the total APS is free from any evident features (see Fig. 12 of Zavala et al. 2010). Nevertheless, the spurious angular periodicity, in addition to the fundamental angular correlation associated with  $\Delta\theta$ , introduces smaller scale harmonics that affect multipoles larger than  $\ell^*$ . Although these additional peaks are much smaller

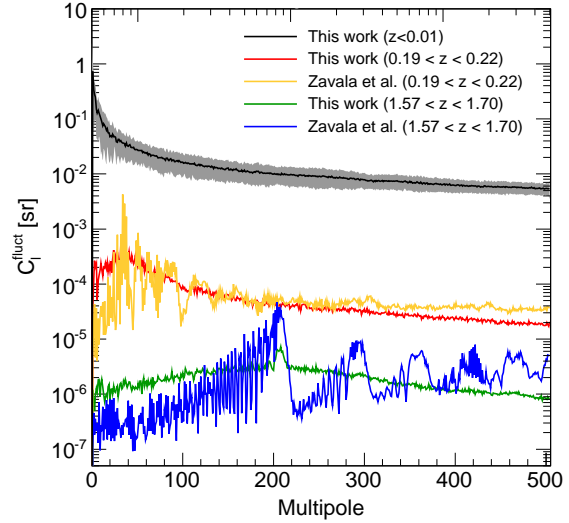


**Figure 2.** Fluctuation APS of anisotropies of the gamma-ray intensity produced by DM annihilating in extragalactic (sub)halos resolved in the MS-II, and located in a shell corresponding to  $z < 0.01$  (black line),  $0.19 < z < 0.22$  (red and yellow lines) and  $1.57 < z < 1.70$  (green and blue lines). Yellow and blue lines refer to the map-making algorithm presented in Zavala et al. (2010), while the black, red and green lines correspond to our improved algorithm; see text for details. The grey band around the black line indicates the  $1\sigma$  standard deviation among 10 different realizations of the first shell ( $z < 0.01$ ).

than the fundamental one, we decided to reduce this spurious effect by randomly rotating and translating every single replica within the past light cone instead of doing so only for every concentric shell.

The improvement of the new method becomes evident in Fig. 2 where we show the comparison between the fluctuation APS<sup>5</sup> (for individual shells) computed with our map-making code (red and green lines) and the original one by Zavala et al. (2010) (yellow and blue lines). The yellow and red lines refer to the shell with  $z = 0.21$ , while the blue and green lines are for  $z = 1.63$ . The small-scale spurious harmonics essentially disappear in the new method and the fundamental mode, although still present, is greatly reduced relative to the previous method.

The map-making code produces realizations of the distribution of DM halos around the observer through random rotations and translations of the MS-II boxes that fill the volume of the past-light cone. In order to quantify the effect of this random component in the simulated signal, we generate 10 different realizations of the first shell (corresponding to  $z < 0.01$ ) and compute the fluctuation APS for each of them. We only consider the effect of having different random rotations for the first shell since it is expected to be more important for nearby resolved structures, while shells at larger redshifts are less affected. In Fig. 2 we plot the average APS over these 10 realizations (black line) as well as the  $1\sigma$  fluctuation (grey band). We can see that the effect induced on the APS is relatively small (at least compared to the other sources of uncertainties introduced later) and we neglect it from now on.

All halos up to  $z = 2$  are considered when computing the extragalactic signal. By this redshift, the cumulative emission has already reached  $\geq 80\%$  of the total signal (in the case of prompt

<sup>4</sup> <http://healpix.jpl.nasa.gov>

<sup>5</sup> The APS will be formally defined in Sec. 5.2.

emission  $\sim 90\%$  of the signal actually comes from  $z < 1$ ; see Fig. 9 of Profumo & Jeltema 2009 and Fig. 11 of Zavala et al. 2010). The first shell of the extragalactic map starts at a distance of  $R_{\min} = 583$  kpc, corresponding to approximately twice the virial radius of the galactic halo. The volume within this distance is filled with the data from the AQ simulation (see Sec. 4).

In the upper panels of Fig. 3 we show the gamma-ray intensity of the EG-MSII component at 4 GeV for the first snapshot ( $z < 0.01$ ), in the case of annihilating DM (left panels,  $m_\chi = 200$  GeV,  $(\sigma_{\text{ann}}v) = 3 \times 10^{-26} \text{cm}^3 \text{s}^{-1}$  and  $B_b = 1$ ) and decaying DM (right panels,  $m_\chi = 2$  TeV,  $\tau = 2 \times 10^{27} \text{s}$  and  $B_b = 1$ ). The characteristic filaments of the cosmic web and individual DM halos are clearly visible, as well as (at least for the case of decaying DM) some subhalos hosted in large DM clumps. In the second row of this figure, we show the intensity up to  $z = 2$ : the map is much more isotropic, even if some of the prominent, closest structures can still be seen.

### 3.2 Unresolved main halos (EG-UNRESMain)

We describe now how we model the contribution of unresolved main halos, (i.e. those with masses below  $M_{\text{res}}$ ), a contribution that we call EG-UNRESMain. Since this is a regime which goes below the MS-II mass resolution, we are forced to resort to some assumptions concerning both the distribution and the individual properties of DM halos. Our approach is similar to the one of Zavala et al. (2010): we use main halos in the MS-II to perform an analytic fit to the single-halo luminosity (i.e.  $L(M)$  defined in Eqs. 4 and 6) as well as to the following function:

$$F(M) = \frac{\sum L(M)}{M \Delta \log M} \approx \ln 10 L(M) \frac{\Delta n(\bar{M})}{\Delta M}, \quad (8)$$

which is the total luminosity of main halos with a mass in the logarithmic mass range  $\log M \pm \Delta \log M/2$ , divided by its mean value  $\bar{M}$  and the width of the logarithmic mass bin. The second equality shows how  $F(M)$  depends on the halo mass function  $\Delta n/\Delta M$  in the bin considered. By extrapolating the fit obtained for  $F(M)$  above  $M_{\text{res}}$ , it is possible to estimate the gamma-ray intensity due to DM main halos below  $M_{\text{res}}$  down to different values of  $M_{\min}$ . In Zavala et al. (2010) (see their Figs. 5 and 6), the authors compared the predictions of such an extrapolation, in the case of annihilation, with the result of an analytical model based on the formalism of Sheth et al. (2001) for the halo mass function and Eke et al. (2001) for the concentration-mass relation. The total flux in unresolved main halos with a mass between  $M_{\min} = 10^{-6} M_\odot/h$  and  $M_{\text{res}}$  agrees within a factor of 5 between the two approaches.

This missing flux is then added to the emission of resolved halos with mass between  $1.39 \times 10^8$  and  $6.89 \times 10^9 M_\odot/h$  (halos with particle number between 20 and 100). The decision to boost up only these halos is equivalent to assuming that halos smaller than  $M_{\text{res}}$  share the same spatial clustering as those within that mass range. This assumption is motivated by the fact that the two-point correlation function of halos approaches an asymptotic value already at these masses (see Fig. 7 of Boylan-Kolchin et al. 2009).

Nevertheless, the actual clustering of low-mass main halos is unknown and, even if they trace the distribution of more massive objects, treating their contribution simply as a boost factor for the halos with lowest masses in the MS-II may overestimate their true clustering. Assuming, instead, that they are distributed more isotropically would reduce their contribution to the total APS (especially at low multipoles), although it is difficult to estimate precisely by how much. In what follows we assume that the uncer-

tainty in the clustering of unresolved main halos is small and can be ignored.

The same procedure described above is also applied for the case of DM decay.

### 3.3 Unresolved subhalos

In this section we describe how we account for the emission from unresolved subhalos, i.e.: *i*) subhalos with masses below  $M_{\text{res}}$  that are hosted by main halos in the MS-II catalogs, and *ii*) subhalos of unresolved main halos. We do not consider sub-subhalos since their contribution is likely negligible in comparison (see, e.g., Martinez et al. 2009). Note also that, at least at low redshifts, most of these subhalos have been removed by tidal stripping (Springel et al. 2008).

For the extragalactic emission, the impact of unresolved subhalos on the intensity and angular anisotropy spectra is essentially to boost the luminosity of the host by a certain amount. Thus, in principle, any method that provides boosts within the range of what has been found previously in the literature is a reasonable one. The method we use here has the advantage of having a single parameter ( $k$  in Eq. 9) that controls the abundance of substructure, which can be easily adjusted to obtain the subhalo boosts that have been reported in the past.

Kamionkowski & Kouhiappas (2008) and Kamionkowski et al. (2010) propose a method to compute the subhalo boost factor for the annihilation rate of a MW-like DM halo, providing an expression for the total boost factor  $B_{\text{ann}}(M_{\text{MW}})$ , as well as the differential profile  $B_{\text{ann}}(M_{\text{MW}}, r)$  (expressing the boost factor at a distance  $r$  from the center of the halo). This prescription was calibrated with the Via Lactea II simulation (Diemand et al. 2008). The distribution of particles in this simulation is used to derive the probability  $P(\rho, r)$  of having a value of the DM density between  $\rho$  and  $\rho + d\rho$  at a distance  $r$  from the center of the main halo. Two different components contribute to  $P(\rho, r)$ : the first one is Gaussian and corresponds to the smooth DM halo, while for higher values of  $\rho$ , the probability is characterized by a power-law tail due to the presence of subhalos (see Fig. 1 of Kamionkowski et al. 2010). The fraction of the halo volume that is filled with substructures is well fitted by<sup>6</sup>:

$$1 - f_s(r) = k \left( \frac{\rho_{sm}(r)}{\rho_{sm}(r = 100 \text{ kpc})} \right)^{-0.26}, \quad (9)$$

with  $k = 7 \times 10^{-3}$ .  $P(\rho, r)$  is then used to derive an expression for the boost factor  $B_{\text{ann}}(r)$  in the case of annihilating DM:  $B_{\text{ann}}(M, r) = \int_0^{\rho_{\text{max}}} d\rho P(\rho, r) \rho^2 / \rho_{sm}^2(r)$ , where  $\rho_{\text{max}}$  is a maximum density, which is of the order of the density of the earliest collapsing subhalos (see below) and  $\rho_{sm}$  is the density of the smooth component.

Sánchez-Conde et al. (2011) extended the previous method to halos of all sizes, adopting a slight modification to the definition of  $f_s(r)$ :

$$1 - f_s(r) = k \left( \frac{\rho_{sm}(r)}{\rho_{sm}(r = 3.56 \times r_s)} \right)^{-0.26}, \quad (10)$$

<sup>6</sup> Since current simulations are many orders of magnitude away from resolving the whole subhalo population down to  $M_{\min}$ ,  $f_s(r)$  is known with limited precision and represents one of the implicit uncertainties of our predictions.



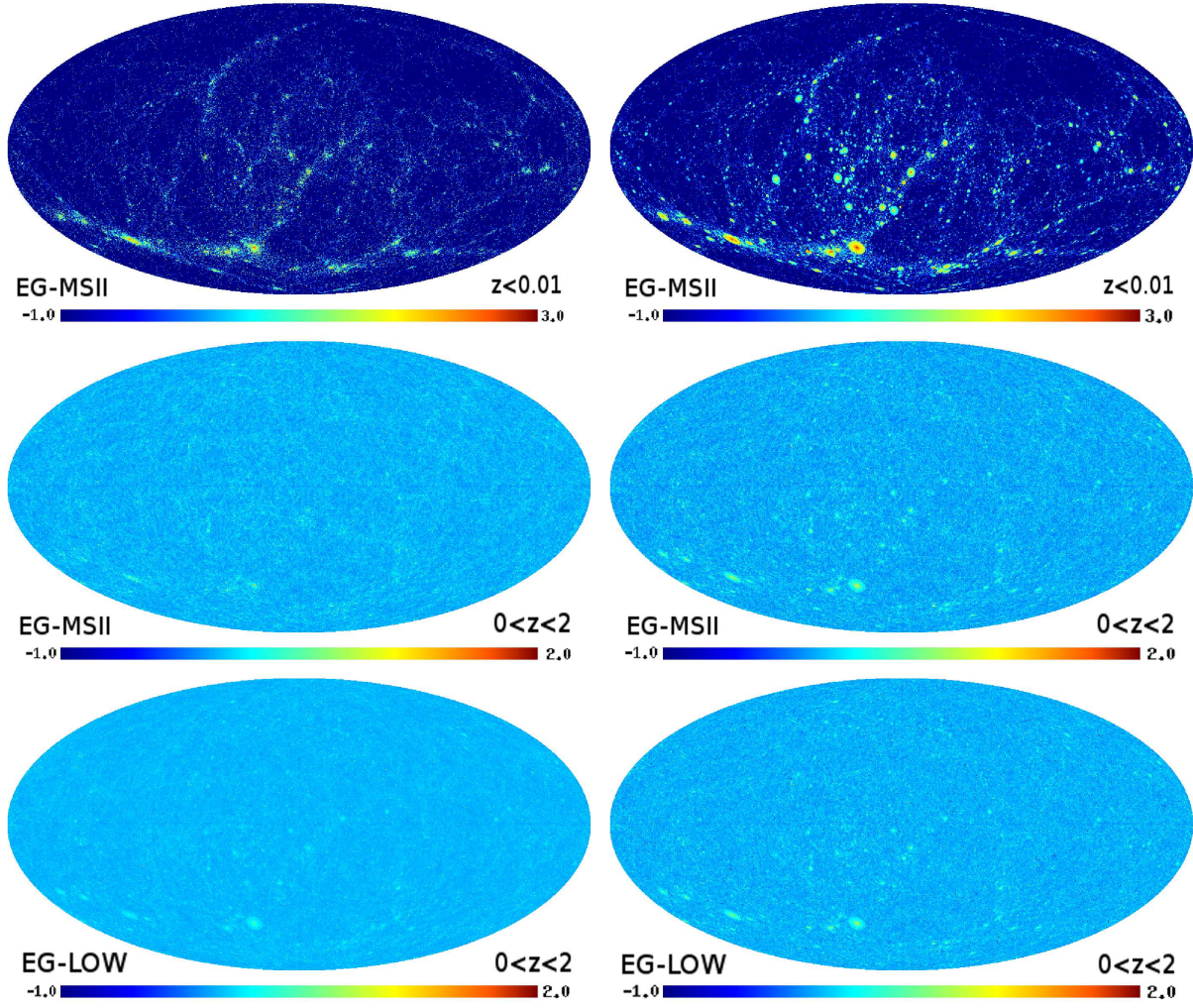


**Figure 3.** All-sky maps of the gamma-ray intensity (in units of  $\text{cm}^{-2}\text{s}^{-1}\text{sr}^{-1}\text{GeV}^{-1}$ ) at 4 GeV from DM annihilation (left panels) and DM decay (right panels). The figure shows the emission of all DM (sub)halos down to the resolution limit of the MS-II (EG-MSII component). In the upper row only nearby structures ( $z < 0.01$ ) are considered, while in the second row the emission up to  $z = 2$  is considered. In the last row we plot the emission from all extragalactic (sub)halos (resolved and unresolved) down to  $M_{\min} = 10^{-6}M_{\odot}/h$  with the LOW subhalo boost (see text for details). In all cases, annihilation or decay into  $b$  quarks is assumed: for annihilating DM,  $m_{\chi} = 200$  GeV with a cross section of  $3 \times 10^{-26}\text{cm}^3\text{s}^{-1}$ , while for decaying DM,  $m_{\chi} = 2$  TeV with a lifetime of  $2 \times 10^{27}\text{s}$ . The photon yield receives contributions from prompt emission and IC off the CMB photons (see Sec. 2). In each map we subtract the all-sky average intensity of that component, after moving to a logarithmic scale. Note the different scales in the first row.

where  $r_s$  is the scale radius of the host halo given in  $\text{kpc}^7$ . We note that this implies that halos of all masses have the same radial dependence of  $f_s$ , only rescaling it to the particular size of the halo. This is partially supported by the mass-independent radial distribution of subhalos found in simulations (e.g. Angulo et al. 2008). Using Eq. 10, Sánchez-Conde et al. (2011) found that  $B_{\text{ann}} < 2$  for the MW dwarf spheroidals, while  $B_{\text{ann}} \sim 30 - 60$  for galaxy clusters (integrating up to the tidal and virial radius, respectively). In both cases, the morphology of the total gamma-ray emission coming from the halo is modified since the subhalo contribution makes the brightness profile flatter and more extended.

For the case of annihilating DM, we account for the contribution of unresolved subhalos by implementing the procedure of Sánchez-Conde et al. (2011) in two different ways:

- for the subhalos of unresolved main halos we integrate  $F_{\text{ann}}(M)B_{\text{ann}}(M)$  to compute the total luminosity from  $M_{\min}$  to  $M_{\text{res}}$ . The result of this integral is then used to boost up the emission of main halos in the MS-II with a mass between  $1.39 \times 10^8$  and  $6.89 \times 10^9 M_{\odot}/h$ .

- for subhalos belonging to main halos that are resolved in the simulation we boost up the luminosity of each halo by the mass-dependent boost  $B_{\text{ann}}(M)$  (i.e. the integral of  $B_{\text{ann}}(M, r)$  up to the virial radius). If the halo is extended, in addition to a total luminosity boost, we assume a surface brightness profile as given by  $B_{\text{ann}}(M, r)$ . We need to apply a correction to this procedure since these equations account for subhalos from a minimum mass  $M_{\min}$  up to the mass of the main halo  $M$ , whereas subhalos with masses above  $M_{\text{res}}$  are resolved and already accounted for in the simulation (they belong to the EG-MSII component). To correct for this double-counting, we simply compute (and subtract) the emission due to subhalos down to a minimal mass equal to  $M_{\min} = M_{\text{res}}$ .

<sup>7</sup> The value of 3.56 is chosen so that, for the MW halo in Via Lactea II, Eqs. 10 and 9 are identical.

We note that changing  $M_{\min}$  corresponds to changing  $\rho_{\max}$ . From Kamionkowski et al. (2010), the maximum density in a halo is the density that its smallest subhalo had at the moment this subhalo formed:

$$\rho_{\max}(M_{\min}) = \frac{200}{12} \frac{c_{200}^3(M_{\min}, z_F)}{f(c_{200}(M_{\min}, z_F))} \rho_{\text{crit}}(z_F), \quad (11)$$

where  $f(x) = \ln(1+x) - x/(1+x)$ . The epoch of collapse  $z_F$  as a function of halo mass can be computed using the spherical collapse model of DM halo formation and evolution (see, e.g., Sánchez-Conde et al. 2007 and references therein), which shows that for low masses, up to  $\sim 1 M_{\odot}/h$ , all halos collapse approximately at the same redshift,  $z_F = 40$ . The initial concentrations are set by the formation epoch, which means that halos that collapse at roughly the same  $z_F$  will have similar  $c_{200}(z_F)$ . Thus, according to Eq. 11, all low-mass subhalos will be characterized roughly by the same  $\rho_{\max} \sim 2.51 \times 10^9 M_{\odot}/\text{kpc}^3$  (for  $M_{\min} < 1 M_{\odot}/h$ , after fixing  $c_{200}(z_F)$  to a constant value of 3.5 as suggested by simulations (e.g. Diemand et al. 2006; Zhao et al. 2009)<sup>8</sup>. We compute  $\rho_{\max}$  for a set of reference values of  $M_{\min}$  (see also Sec. 6.4, noting that  $z_F > 5$  for  $M_{\min} \lesssim 10^9 M_{\odot}/h$ , which implied that we can safely assume  $c_{200}(z_F) = 3.5$  (Zhao et al. 2009). Note also that, by using the case of  $M_{\min} = M_{\text{res}} = 6.89 \times 10^9 M_{\odot}/h$  we can correct for the aforementioned problem of double-counting the subhalos with masses above the MS-II mass resolution.

Recently, Pinzke et al. (2011) and Gao et al. (2011) also estimated the substructure boost for DM halos of mass ranging from those of dwarf spheroidals to those of galaxy clusters. They point to substantially larger boost factors than those found by Sánchez-Conde et al. (2011) for the same mass range. This is mainly a consequence of the different methodologies. In the former cases, the subhalo mass function and the concentration-mass relation are power-laws calibrated at the resolved masses and extrapolated to lower unresolved masses. On the contrary, in the method by Kamionkowski et al. (2010) (with the modification implemented in Sánchez-Conde et al. 2011), the dependence on  $M_{\min}$  is flatter towards lower masses due to the limit on the natal concentrations.

Nevertheless, using the procedure described in the previous paragraphs, we can obtain similar subhalo boosts to those given by Pinzke et al. (2011) and Gao et al. (2011) if we *substantially* increase the parameter that controls the abundance of substructure in Eq. 10 to  $k = 0.15$ . Both cases ( $k = 7 \times 10^{-3}$  as in Sánchez-Conde et al. 2011, and  $k = 0.15$  to reproduce the results of Pinzke et al. 2011 and Gao et al. 2011) are considered in this paper as representative of scenarios with a small and a large subhalo boost and are referred in the following as the LOW and HIGH scenarios, respectively. These two cases represent the extreme values reported in the literature for the contribution of unresolved subhalos. By obtaining predictions for the total DM-induced emission for these extrema, we aim at estimating how large is the uncertainty associated with the unresolved subhalo population. Parameterizing such uncertainty in this way represents a “hybrid” approach, since it does not rely completely either on a direct extrapolation of the results of simulations (Zavala et al. 2010) or on analytical estimates such as the stable clustering hypothesis (Afshordi et al. 2010).

Up to now, the discussion of how to model unresolved subhalos refers only to the case of annihilating DM. For decaying DM,

there is no need to model this contribution since these subhalos are too small to be detected by the subhalo finder and their mass is already accounted for in the mass of the host halo. Since for decaying DM the total luminosity of a halo is proportional to its mass, the unresolved subhalos contribute to what we call the “smooth component”<sup>9</sup>. This is strictly valid only if we consider the total halo luminosity. If the intensity profile is needed, we should consider that the true spatial distribution of unresolved subhalos is expected to be different from that of the smooth component. In the case of the extragalactic emission we neglect this effect since only the halos that are close by appear extended in the maps, while the vast majority appear as point sources. For the case of the galactic emission we comment on this issue on Sec. 4.2.

## 4 THE GAMMA-RAY EMISSION FROM THE MILKY-WAY HALO

### 4.1 The smooth Milky-Way halo

Our model for the emission from the smooth DM halo of our own galaxy is partially based on the results of the Aquarius project (Springel et al. 2008; Navarro et al. 2008). With the goal of studying the evolution and structure of MW-size halos, the Aquarius project selected a group of MS-II halos with properties similar to the MW halo and resimulated them at increasing levels of resolution. The different AQ halos are characterized by virial masses between  $0.95$  and  $2.2 \times 10^{12} M_{\odot}/h$  and have a variety of mass accretion histories (Boylan-Kolchin et al. 2010). In this sense, they are not expected to be a perfect match to the dynamical properties of our own MW halo, but rather to be a representative sample of MW-size halos within the context of the CDM paradigm. We consider here the halo dubbed Aq-A-1, containing more than one billion particles within  $r_{200}$  and having a mass resolution of  $1250 M_{\odot}/h$ . A careful analysis of the density profile of the smooth component of the Aq-A-1 halo performed by Navarro et al. (2008) shows that the simulation data is best fitted by an Einasto profile (preferred over an NFW profile):

$$\ln\left(\frac{\rho(r)}{\rho_{-2}}\right) = \left(\frac{-2}{\alpha}\right) \left[\left(\frac{r}{r_{-2}}\right)^{\alpha} - 1\right], \quad (12)$$

with  $r_{-2} \sim 15.14$  kpc,  $\rho_{-2} = 3.98 \times 10^6 M_{\odot}/\text{kpc}^3$  and  $\alpha \sim 0.170$ .

Stellar dynamics and microlensing observations can be used to constrain the absolute value of the DM density at the position of the Earth,  $\rho_{\text{loc}}$ . Different results point towards a range of values between  $0.2$  and  $0.5 \text{ GeV}/\text{cm}^3$  (Prada et al. 2004; Catena & Ullio 2010; Pato et al. 2010; Salucci et al. 2010; Iocco et al. 2011). Noting that a different value for the local DM density would shift up or down our predictions for the intensity of the emission from DM annihilation/decay in the MW smooth halo proportionally to  $\rho_{\text{loc}}^2$  and  $\rho_{\text{loc}}$ , respectively, we decide to renormalize the value of  $\rho_{-2}$  of Aq-A-1 in order to reproduce a reference value of  $\rho_{\text{loc}} = 0.3 \text{ GeV}/\text{cm}^3$  (a similar approach was used in Pieri et al. 2011).

To build our template map for the smooth MW halo, we assume that the observer is located at the solar circle at a distance of  $8.5$  kpc from the GC and we integrate the DM-induced emission

<sup>8</sup> Here, a matter power spectrum parametrized as in Bardeen et al. (1986) was used to compute  $z_F$ , with the most recent values of the cosmological parameters and with no exponential cut-off at the minimal mass of DM halos.

<sup>9</sup> For the case of DM annihilation note that, although the mass of unresolved subhalos is also accounted for as part of the “smooth component”, this does not imply that their contribution to the gamma-ray intensity is already considered since the annihilation rate is not proportional to the DM density, but to the density squared.



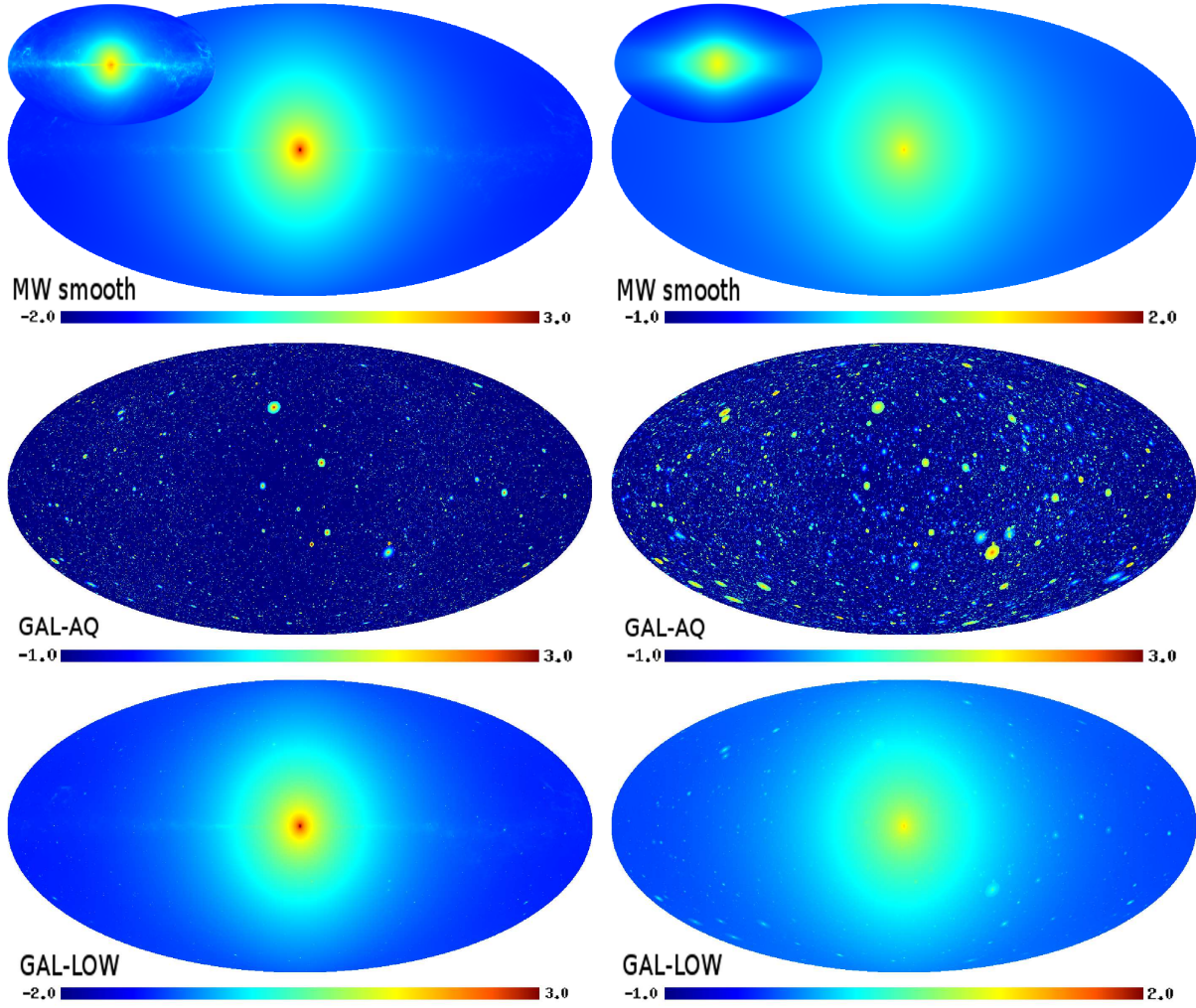


**Figure 4.** All-sky map of the galactic gamma-ray intensity (in units of  $\text{cm}^{-2}\text{s}^{-1}\text{sr}^{-1}\text{GeV}^{-1}$ ) at 4 GeV from DM annihilation (left panels) and decay (right panels). In the first row, we show the emission from the smooth MW halo, while the contribution of resolved subhalos in the Aquarius Aq-A-1 halo (GAL-AQ component) is shown in the second row. The maps on the last row indicate the total galactic emission accounting for the MW smooth halo and its (resolved and unresolved) subhalos down to  $M_{\min} = 10^{-6} M_{\odot}/h$  (for the LOW subhalo boost). As in Fig. 3,  $m_{\chi} = 200$  GeV, the cross section is  $3 \times 10^{-26} \text{cm}^3 \text{s}^{-1}$  and  $B_b = 1$  for the left panels, while  $m_{\chi} = 2$  TeV with a lifetime of  $2 \times 10^{27} \text{s}$  and  $B_b = 1$  for the right ones. The intensity includes contributions from prompt emission and IC with the CMB photons (see Sec. 2). For the emission of the MW smooth halo we also consider IC with the complete ISRF, as well as hadronic emission. The non-prompt emission alone is shown in the smaller panels overlapping with the maps of the first row. In each map we subtract the all-sky average intensity of that component, after moving to a logarithmic scale. Note the different scale in the different panels.

along the line of sight up to a distance of 583 kpc ( $\sim 2.5 r_{200}$  of Aq-A-1). This distance marks the transition between our galactic and extragalactic regimes and it is selected because the Aq-A-1 halo is still simulated with high resolution up to this radius, and it therefore provides a better representation of the outermost region of the MW halo than the MS-II. For the smooth component, in addition to the prompt emission and secondary emission from IC scattering with the CMB photons, we also consider the emission due to IC scattering with the complete InterStellar Radiation Field (ISRF) provided in Moskalenko et al. (2006) as well as hadronic emission from interactions with the interstellar gas (see Appendices A and B for details). The first row in Fig. 4 shows the gamma-ray emission from DM annihilation (left panel) and decay (right panel) in the smooth MW halo. The secondary emission correlated with the MW ISRF and the interstellar gas can be seen along the galactic plane and is plotted independently in the small panels overlapping with the maps of the first row.

## 4.2 The Milky Way subhalos (GAL-AQ and GAL-UNRES)

This section focuses on the contribution of galactic subhalos, dealing with *i*) subhalos that are resolved in the Aq-A-1 halo, (which we refer to as the GAL-AQ component) and *ii*) subhalos with masses below the mass resolution of AQ (which we call the GAL-UNRES component). As we did in Sec. 3.1, we use the subhalo catalog to compute the luminosity of each object from its  $V_{\max}$  and  $r_{\max}$  values<sup>10</sup>. Only subhalos with more than 100 particles are considered, resulting in an “effective” AQ mass resolution of  $1.71 \times 10^5 M_{\odot}$ . The gamma-ray intensity in a given direction  $\Psi$  is then obtained by summing up the contribution from all subhalos encountered along the line of sight, up to a distance of 583 kpc. The GAL-AQ compo-

<sup>10</sup> As in the case of extragalactic (sub)halos, we correct the values of  $V_{\max}$  and  $r_{\max}$  for numerical effects (see Sec. 3.1).

nent is shown in the second row of Fig. 4 in the case of annihilation (left) and decay (right).

For an annihilating DM candidate, the contribution of unresolved galactic subhalos is accounted for using the same procedure as for unresolved extragalactic subhalos described in Sec. 3.3, introducing the LOW and HIGH cases as representatives of scenarios with a small and a large subhalo annihilation boost. The LOW boost is taken again directly from Kamionkowski et al. (2010) and Sánchez-Conde et al. (2011) (which assumes  $k = 7 \times 10^{-3}$ ), while the HIGH boost is tuned to reproduce the results of Springel et al. (2008) who estimated a total subhalo boost of 232 (integrating up to  $r_{200}$  for the Aq-A-1 halo and for  $M_{\min} = 10^{-6} M_{\odot}/h$ ); we reproduce this result using  $k = 0.2^{11}$ .

In the case of decaying DM, we note that the mass contained in resolved subhalos is  $2.7 \times 10^{11} M_{\odot}$  ( $\sim 15\%$  of  $M_{200}$  for the Aq-A-1 halo, if we consider subhalos down to  $1.71 \times 10^5 M_{\odot}$ , see Eq. 5 of Springel et al. (2008)). This goes up to  $3.9 \times 10^{11} M_{\odot}$  if we extrapolate the subhalo mass function down to  $M_{\min} = 10^{-6} M_{\odot}/h$ , which implies that unresolved subhalos contribute to the halo mass (and hence to the total decay luminosity) slightly less than resolved ones (see end of Sec. 3.3). Thus, an upper limit to the gamma-ray intensity from DM decay coming from these unresolved subhalos can be obtained by considering the flux coming from resolved subhalos, which is less than 1% of the flux coming from the smooth component. Hence, we decide to ignore the contribution of unresolved subhalos to the amplitude of the galactic DM-decay emission.

Regarding the contribution to the APS from unresolved subhalos, we note that although subhalos just below the mass resolution of Aq-A-1 ( $\sim 10^5 M_{\odot}$ ) might still contribute to the anisotropies, mainly through a Poisson-like APS, their abundance is so large (the subhalo mass function grows as  $\propto M^{-1.9}$ ) that the intrinsic anisotropies of the gamma-ray intensity produced by them would be very small. Because of this, the APS at multipoles above  $l \sim 100$  is likely dominated by subhalos with masses above  $10^5 M_{\odot}$  (see Sec. 5.2 and the top panel of Fig. 8 of Ando 2009), allowing us to neglect the contribution of subhalos with lower masses. We have verified this is indeed the case using the analytical model of Ando (2009) (see discussion in Sec. 5.2.2 and Appendix D).

We do not take into account annihilation boosts due to fine-grained phase-space structures like streams and caustics. For a standard DM model without specific boost mechanisms (e.g. Sommerfeld enhancement) these effects are subdominant (Vogelsberger et al. 2007; White & Vogelsberger 2008; Vogelsberger et al. 2009; Vogelsberger & White 2010). If a mechanism like the Sommerfeld enhancement is invoked, fine-grained streams increase significantly the main halo annihilation, but their contribution is typically still less than that from subhalos (Zavala et al. 2011).

Finally, in Tab. 1 we summarize the nomenclature used to identify the different components of DM-induced extragalactic and galactic emission introduced in the present section and in the previous one.

Name	Description
EG-MSII	DM halos and subhalos in MS-II catalogs with more than 100 particles (i.e. with a mass larger than $M_{\text{res}} = 6.89 \times 10^9 M_{\odot}/h$ )
EG-UNRESMain	extragalactic DM (main) halos with a mass between $M_{\min}$ and $M_{\text{res}} = 6.89 \times 10^8 M_{\odot}/h$
EG-LOW	resolved and unresolved (sub)halos down to $M_{\min}$ . The unresolved subhalos are simulated following Sánchez-Conde et al. (2011) with $k = 7 \times 10^{-3}$ (includes EG-MSII and EG-UNRESMain)
EG-HIGH	resolved and unresolved (sub)halos down to $M_{\min}$ . The unresolved subhalos are simulated following Sánchez-Conde et al. (2011) with $k = 0.15$ (includes EG-MSII and EG-UNRESMain)
MW smooth	smooth MW DM halo, parametrized by an Einasto profile as in Navarro et al. (2008), and normalized to a local DM density of $0.3 \text{ GeV/cm}^3$
GAL-AQ	DM subhalos in the AQ catalogs with more than 100 particles (i.e. with a mass larger than $1.71 \times 10^5 M_{\odot}$ )
GAL-UNRES (LOW)	DM subhalos with a mass between $M_{\min}$ and $1.71 \times 10^5 M_{\odot}$ , simulated following Sánchez-Conde et al. (2011) with $k = 7 \times 10^{-3}$
GAL-UNRES (HIGH)	DM subhalos with a mass between $M_{\min}$ and $1.71 \times 10^5 M_{\odot}$ , simulated following Sánchez-Conde et al. (2011) with $k = 0.2$
GAL-LOW	MW smooth + GAL-AQ + GAL-UNRES (LOW)
GAL-HIGH	MW smooth + GAL-AQ + GAL-UNRES (HIGH)

**Table 1.** Summary table of the nomenclature used in the paper to identify the different components of the DM-induced emission.

## 5 ENERGY AND ANGULAR POWER SPECTRA OF THE DARK-MATTER-INDUCED GAMMA-RAY EMISSION

Before showing the analysis of our simulated maps, we note that changing the particle physics scenario (i.e. considering a different value for  $m_{\chi}$  and/or selecting a different annihilation/decay channel) would require, in principle, re-running our map-making code for the extragalactic intensity, since the photon emission spectrum is redshifted along the line of sight. This is a computationally expensive task given that one complete realization takes approximately 50000 CPU hours. However, this is not necessary since it is possible, given a reference all-sky map obtained for a particular particle physics model, to derive the corresponding map for a different model simply applying a set of re-normalization factors for different redshifts. Such prescription is described in detail in Appendix C.

<sup>11</sup> The formalism by Kamionkowski et al. (2010) overestimates the subhalo abundance in the inner region of the MW-like halo, namely within 20 kpc. To correct for this, we assume that within this radius, the spatial distribution of unresolved subhalos follows the AQ distribution, being well fitted by an Einasto profile with  $\alpha = 0.678$  and  $r_{-2} = 199$  kpc.

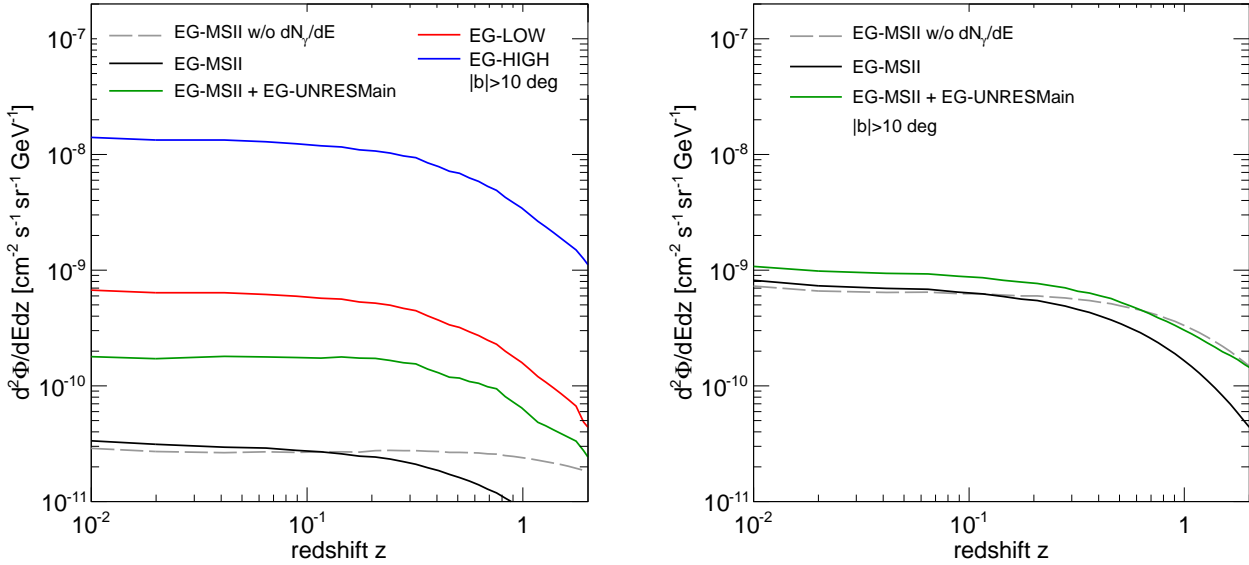


**Figure 5.** Average of the extragalactic gamma-ray intensity per unit of redshift as a function of redshift at 4 GeV from DM annihilation (left panel) and DM decay (right panel) for  $|b| > 10^\circ$ . Solid black lines correspond to the contribution from resolved (sub)halos in the MS-II (EG-MSII), while the solid green lines include in addition the boost from unresolved main halos (EG-UNRESMain, see Section 3.2). The solid red and blue lines include all the previous components and the emission from unresolved subhalos down to a minimum mass  $M_{\min} = 10^{-6} M_\odot$  according to the method described in Section 3.3 for the LOW and HIGH case, respectively. In all cases, annihilation or decay into bottom quarks is assumed: for annihilating DM,  $m_\chi = 200$  GeV and  $(\sigma_{\text{ann}} v) = 3 \times 10^{26} \text{ cm}^3 \text{ s}^{-1}$ , while for decaying DM,  $m_\chi = 2$  TeV and  $\tau = 2 \times 10^{27} \text{ s}$ . The photon yield receives contributions from prompt emission and IC of the CMB photons. The dashed grey line shows the “astrophysical” part of the signal (with an arbitrary normalization) for the EG-MSII component, by neglecting the  $dN_\gamma/dE$  factor in Eqs. 1 and 2.

## 5.1 Analysis of the energy spectrum

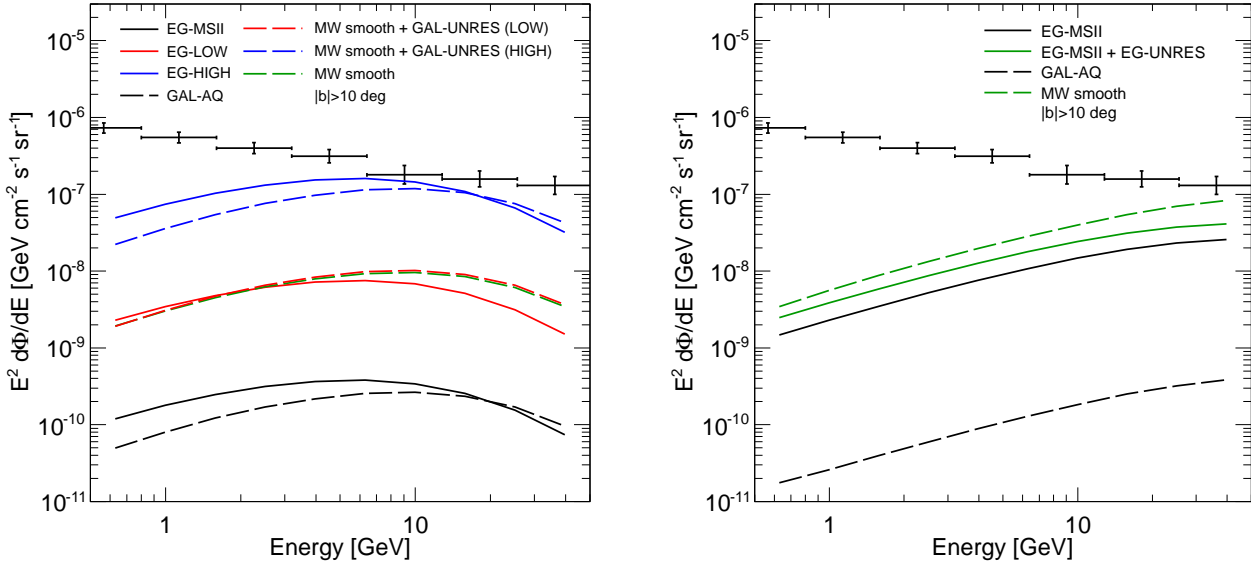
### 5.1.1 Extragalactic emission

Fig. 5 shows the average DM-induced gamma-ray intensity per unit redshift of our simulated extragalactic maps as a function of redshift (left and right panels for DM annihilation and DM decay, respectively), for an energy of 4 GeV. The average is computed over the whole sky except for a strip of  $10^\circ$  along the galactic plane, since this is the region used in Abdo et al. (2010c) to determine the Fermi-LAT IGRB energy spectrum. Note that the intensity in each concentric shell filling up the volume of the past light cone is divided by the width of the particular shell in redshift space  $\Delta z$ : this is roughly equivalent to computing the average of the integrand of Eqs. 1 and 2 over the redshift interval of each shell. The intensity from extragalactic resolved (sub)halos in the MS-II (EG-MSII) is shown with a solid black line. This same contribution is shown with a dashed grey line once the photon yield  $dN_\gamma/dE$  is removed from the intensity (arbitrary normalization) in Eqs. 1 and 2, leaving only the “astrophysical” part of the signal. In the case of annihilation, the grey line is essentially flat, with all redshifts contributing equally to the gamma-ray intensity (see also Fig. 1 of Abdo et al. 2010a). Note that, in principle, the EBL attenuation should be visible in the shape of the grey dashed line, but at 4 GeV its effect is negligible and the line only depends on how the DM distribution changes with  $z$ . In the case of decaying DM, the astrophysical part of the signal drops more quickly with redshift since it is proportional to the DM density (which in average grows as  $\propto (1+z)^3$ ) instead of to the density squared. Once the modulation of the photon yield  $dN_\gamma/dE$  is included, we see that the majority of the signal comes from low redshifts (more so for decaying DM): in order to

contribute to the emission at 4 GeV, photons coming from higher redshifts need to be more energetic, and their intensity is damped due to a lower photon yield. For the benchmark shown in Fig. 5, the signal drops by a factor of  $\sim 3 - 5$  from  $z = 0$  to  $z = 1$ .

Once the EG-MSII component is boosted up to include the contribution of unresolved main halos (EG-UNRESMain) with masses down to  $M_{\min} = 10^{-6} M_\odot/h$ , the signal increases by a factor of  $\sim 7$  ( $\sim 1.5$ ) in the case of DM annihilation (decay). The contribution of unresolved main halos is given by integrating  $F_{\text{ann}}(M)$  and  $F_{\text{decay}}(M)$  in Eq. 8 from  $M_{\min}$  to  $M_{\text{res}}$ . These cumulative luminosities are ultimately connected to the halo mass function and the single-halo luminosities  $L_{\text{ann}}(M)$  and  $L_{\text{decay}}(M)$  in Eqs. 4 and 6. Interestingly, they combine to produce a mass-dependent contribution that diverges towards lower masses in the case of DM annihilation ( $F_{\text{ann}}(M) \propto M^{-1.04}$ ), but converges in the case of DM decay ( $F_{\text{decay}}(M) \propto M^{-0.92}$ ). This is the reason why the EG-UNRESMain component is much larger than the resolved component in the case of annihilating DM, while the two remain rather similar for decaying DM. This implies that for the case of decay, the signal is essentially independent of  $M_{\min}$ , as long as  $M_{\min}$  is low enough (see below).

The total emission is obtained by summing the previous components and the contribution of unresolved subhalos down to  $M_{\min}$ . The LOW (red line) and HIGH (blue line) scenarios in the left panel bracket the uncertainty associated with the subhalo contribution, for a fixed value of  $M_{\min} = 10^{-6} M_\odot/h$ . We can see that unresolved (sub)halos boost the signal by a factor between 25 and 400 compared to the EG-MSII component. As noted before, such uncertainty is not present in the case of decaying DM, since the contribution of unresolved (sub)halos is essentially negligible. Note that



**Figure 6.** Average of the gamma-ray intensity coming from DM annihilation (left) and DM decay (right) as a function of observed energy for  $|b| > 10^\circ$ . Solid lines are for the extragalactic contribution, while dashed lines are for the galactic one. The color coding for the solid lines is the same as in Fig. 5, while for the dashed lines, the green one indicates the contribution of the smooth MW halo, the black one is for resolved subhalos (GAL-AQ) and the red and blue lines indicate the emission from the MW smooth halo and its unresolved subhalos (GAL-UNRES) in the LOW and HIGH case respectively (only for the left panel). The observational data points with error bars refer to the measurement of the IGRB as given in Abdo et al. (2010c).

the subhalo boost is smaller at high redshifts since the number of massive resolved main halos decreases with redshift and hence, the overall subhalo boost decreases as well.

Fig. 6 shows the energy spectrum of the average amplitude of the extragalactic (solid lines) DM-induced gamma-ray intensity. We only consider an energy range between 0.5 GeV and 50 GeV, approximately the same range where the IGRB Fermi-LAT data are available (Abdo et al. 2010c). As in Fig. 5, the average is computed in the region with  $|b| > 10^\circ$ . The left (right) panel is for annihilating (decaying) DM. The color-coding of the solid lines is the same as in Fig. 5. The full extragalactic signal, including resolved and unresolved (sub)halos, is expected to lie between the solid red and blue lines.

In the case of DM annihilation, the extragalactic contribution is dominated by unresolved (sub)halos. This prediction agrees well with those from previous works. For instance, the grey band in Fig. 2 of Zavala et al. (2011) can be compared with our “uncertainty” range bracketed by the red and blue lines<sup>12</sup>. To be precise, the methodology implemented in the present paper and the one in Zavala et al. (2011) are not identical, since the emission of unresolved subhalos is accounted for in a different way. Nevertheless, we find that the range covered between our LOW and HIGH subhalo boosts is similar to those reported in Fig. 2 of Zavala et al. (2011) (see also Abdo et al. 2010a).

### 5.1.2 Galactic emission

In Fig. 6 we also show the galactic DM gamma-ray intensity, receiving contributions from the resolved subhalos of the Aq-A-1

halo (GAL-AQ, black dashed line), the smooth MW halo (green dashed line), and from unresolved subhalos (down to  $M_{\min} = 10^{-6} M_\odot/h$ , red and blue dashed lines, for annihilating DM). We see that the emission from resolved galactic subhalos is essentially negligible, indeed being roughly two orders of magnitude smaller than the one from the smooth component (both for annihilating and decaying DM). The effect of unresolved subhalos is important only for DM annihilation and it is estimated to be between less than a factor of 2 (LOW, dashed red) and 10 (HIGH, dashed blue) times more than the smooth component. This represents an important difference with respect to what is found for the extragalactic case, where the subhalo boost can be even larger than two orders of magnitude. It can, however, be understood by noting that for the extragalactic case a given main halo and its subhalos are located essentially at the same distance from the observer, while for the galactic case, the observer is located much closer to the GC than to the bulk of the subhalo emission (on the outskirts of the halo). This is something that has already been noted by Springel et al. (2008), where the subhalo boost to the smooth component of the Aq-A-1 halo (down to  $M_{\min} = 10^{-6} M_\odot/h$ ) was estimated to be 1.9, whereas for a distant observer it was 232. The value of 1.9 is smaller than what we find for the HIGH case, even if the total boost of 232 for the case of a distant observer is compatible with our value. This is due to the slightly different radial distribution of the unresolved subhalos in the HIGH scenario, compared to what is found in Springel et al. (2008).

In the case of decaying DM, the gamma-ray intensity is dominated by the smooth component (approximately compatible with the results of Ibarra et al. 2010).

Comparing the total galactic and extragalactic contributions, we see that they are of the same order for the energy range and an-

<sup>12</sup> Note, however, that although the DM particle mass and the annihilation channel are the same, the annihilation cross section in Fig. 2 of Zavala et al. (2011) is a factor of 5 lower than the one we use in Fig. 6.

nihilation/decay channel explored in Fig. 6<sup>13</sup>. This is roughly consistent with what has been reported previously (e.g. see Fig. 3 of Abdo et al. 2010a, and also Figs. 1 and 2 of Hutsi et al. 2010).

For the particular DM candidates explored in Fig. 6, the total DM-induced emission is able to account for the observed IGRB intensity if the HIGH subhalo boost is considered (at least in one energy bin).

## 5.2 Analysis of the angular power spectrum of anisotropies

We consider now the statistical properties of the anisotropies of our simulated maps, which is the main objective of the present paper. Two slightly different definitions of the APS will be used: *i*) the so-called “intensity APS” ( $C_\ell$ ), defined from the decomposition in spherical harmonics of the two-dimensional sky map after subtracting the average value of the intensity over the sky region considered:

$$\begin{aligned}
 \Delta_{\text{flux}}(\Psi) &= \frac{d\Phi}{dE}(\Psi) - \left\langle \frac{d\Phi}{dE} \right\rangle = \sum_{l=0}^{\infty} \sum_{m=-l}^l a_{lm} Y_{lm}^*(\Psi), \\
 C_\ell &= \frac{1}{2\ell+1} \left( \sum_{|m| \leq \ell} |a_{\ell m}|^2 \right), \quad (13)
 \end{aligned}$$

and *ii*) the so-called “fluctuation APS” ( $C_\ell^{\text{fluct}}$ ), which is dimensionless and is obtained from the decomposition of the *relative* fluctuations of an all-sky map. The fluctuation APS can be obtained from the intensity one simply dividing by  $\langle d\Phi/dE \rangle^2$ .

The intensity APS has the advantage of being an additive quantity, meaning that the intensity APS of a sum of maps is the sum of the intensity APS of each individual component (assuming that the maps are uncorrelated, otherwise their cross-correlations should also be taken into account). On the other hand, the fluctuation APS of multiple components can be summed only after multiplying by the square of the relative emission of each component with respect to the total:

$$C_\ell^{\text{fluct}} \equiv \left\langle \frac{d\Phi}{dE} \right\rangle^{-2} C_\ell = \sum_i \frac{\langle d\Phi^i/dE \rangle^2}{\langle d\Phi/dE \rangle^2} C_{\ell,i}^{\text{fluct}} = \sum_i f_i^2 C_{\ell,i}^{\text{fluct}}. \quad (14)$$

In order to compare directly the APS from our maps with the Fermi-LAT APS measurement, it would be necessary to consider the same target region as in Ackermann et al. (2012a), masking out the known point sources and the region along the galactic plane ( $|b| \leq 30^\circ$ ), where the contamination due to the galactic foreground emission is larger. In this work we only present the APS as obtained directly from our maps and leave the comparison to the Fermi-LAT APS data for future work.

We use HEALPix to compute the APS of our template maps, and note that the APS is conventionally plotted once multiplied by  $\ell(\ell+1)/2\pi$ , which for large multipoles is proportional to the variance of  $\Delta_{\text{flux}}$  (see Eq. 35 of Zavala et al. 2010).

### 5.2.1 Extragalactic APS

The upper panels of Fig. 7 show the fluctuation APS of our template maps at an observed energy of 4 GeV for the case of annihilating DM (left panel) and decaying DM (right panel), using the same particle physics benchmark models used in Figs. 5 and 6 (defined in

Sec. 2). The color-coding is also the same as Fig. 5: solid lines indicate extragalactic components, while dashed ones stand for galactic ones. The minimal halo mass is assumed to be  $M_{\text{min}} = 10^{-6} M_\odot/h$ .

The fluctuation APS (upper panels) illustrates clearly the difference in the intrinsic anisotropies pattern of the different components which can be summarized as follows<sup>14</sup>:

*Resolved (sub)halos in MS-II (EG-MSII)*: in the case of DM annihilation, the extragalactic signal from the resolved (sub)halos (solid black line) is less steep than a pure shot-noise power spectrum, characteristic of perfectly unclustered sources and, not surprisingly, it is in agreement with the results found by Zavala et al. (2010) (see the black solid line of their Fig. 12). At large multipoles, this component is approximately compatible also with the top right panel of Fig. 2 of Ando et al. (2007b).

*Unresolved subhalos of MS-II main halos*: the solid yellow and purple lines correspond to the case in which the emission of resolved main halos is boosted up by the contribution of unresolved subhalos, for the LOW and HIGH subhalo boosts, respectively. We see that at large angular scales, where the APS is related to the clustering of main halos, the yellow and purple lines have a larger normalization than the black one, although their shapes are approximately the same. This is because subhalos give a larger boost to the most massive halos, which are also more clustered (biased). At intermediate scales, from  $\ell = 30$  to 100, the APS gets shallower reflecting the internal distribution of subhalos within the largest halos, which is considerably less peaked than their smooth density profiles. Finally, at larger multipoles ( $\ell > 100$ ), the emission is dominated by low-mass main halos and thus the yellow and violet solid lines are essentially on top of the solid black line.

*Unresolved main halos (EG-UNRESMain)*: on the other hand, the solid green line indicates the case in which the contribution from unresolved main halos is added to the resolved component. The fluctuation APS of the EG-UNRESMain component alone is characterized by a lower normalization than the solid black line, since we assume that unresolved main halos have the same distribution of the least massive halos in MS-II (see Sec. 3.2). Moreover, these are mainly point sources (and very numerous), thus their APS is less steep than the case of the EG-MSII component, being mainly sensitive to what is called the “2-halo term”, i.e., to correlations between points in different halos (e.g. Ando & Komatsu 2006). The green line can be compared with the dashed line in Fig. 12 of Zavala et al. (2010): we note a significant difference for  $\ell > 40$ , where the APS in Zavala et al. (2010) is closer to a pure shot-noise behaviour. This difference already appears in Fig. 2 where the APS obtained with the code used in Zavala et al. (2010) exhibits more power at large multipoles than what we find with our improved map-making code. We speculate that the steep APS of the dashed line in Fig. 12 of Zavala et al. (2010) is a consequence of the spurious features that can be seen in Fig. 2 and that we have reduced in the present work. *Total extragalactic emission*: once the unresolved subhalo boost is applied to halos below and above the MS-II mass resolution, we obtain the full extragalactic emission, for either the LOW (solid red line) or HIGH (solid blue line) subhalo cases. The contribution of unresolved halos (even with the subhalo boost) to the fluctuation APS is subdominant and the shape of the solid red and blue lines is exactly the same as the solid yellow and purple lines, respectively. The decrease in the normalization is due to the fact that the

<sup>13</sup> Notice the slightly different shapes of the energy spectra of the extragalactic and galactic components due to redshifting and photon absorption at high energies in the case of extragalactic objects.

<sup>14</sup> We remind the reader that the extragalactic APS is affected by a deficit of power at large angular scales due to finite size of the MS-II box.



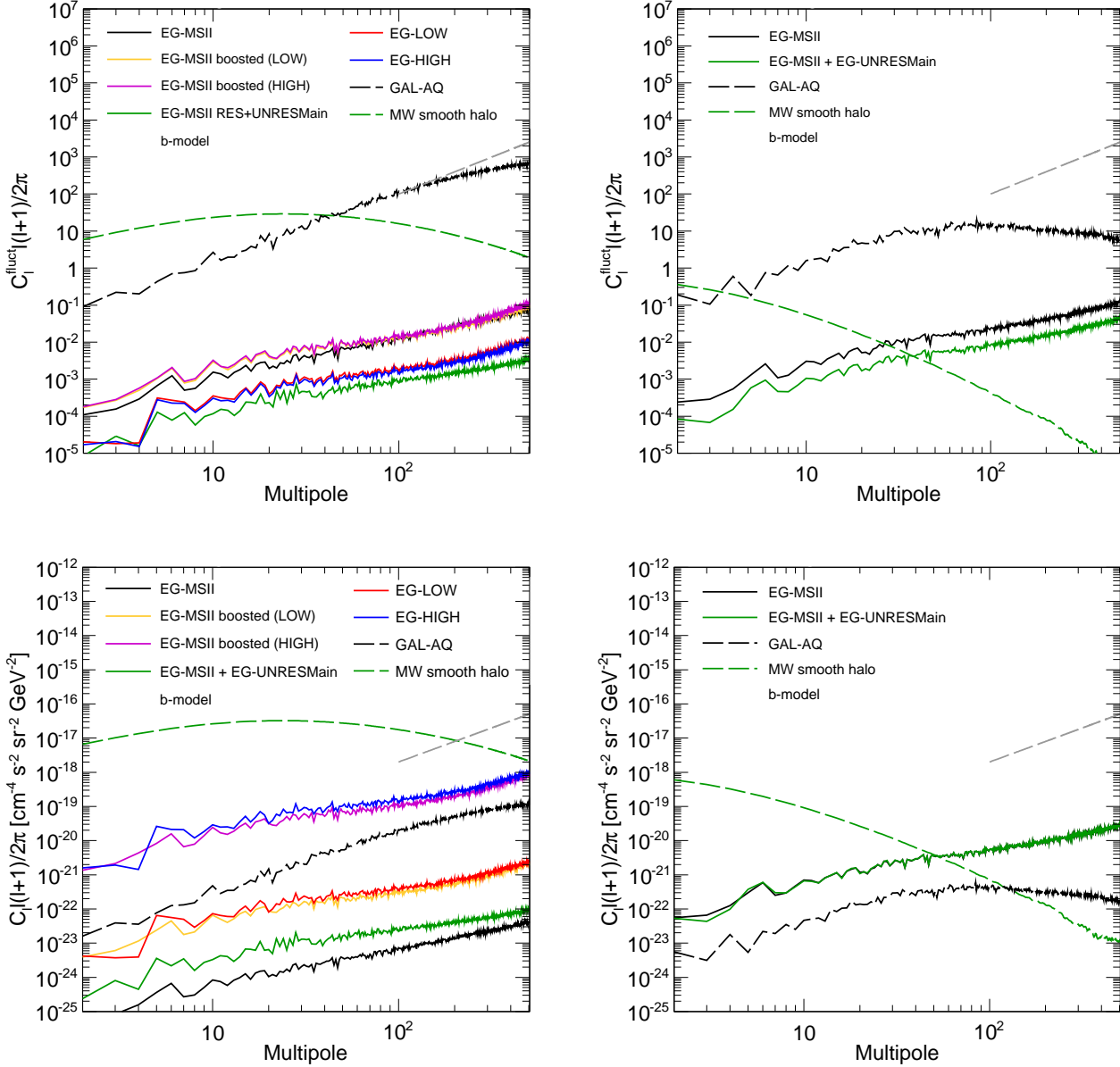


**Figure 7.** Upper panels: Fluctuation APS of the template gamma-ray maps at an observed energy of 4 GeV for annihilating DM (left) and decaying DM (right). The particle physics parameters (including  $M_{\min}$ ) as well as the color coding are the same as those in Figs. 5 and 6. Solid (dashed) lines indicate the extragalactic (galactic) emission. Bottom panels: The same as the upper panels but for the intensity APS (see Eq. 13). The upper panels give a measure of the relative anisotropies of the different components, whereas the bottom panels are an absolute measurement of the anisotropies and clearly show which components dominate the APS. The grey dashed line (with arbitrary normalization) indicates a Poissonian APS independent on multipole.

resolved structures generate anisotropies that only contribute to a small fraction of the total emission (the  $f_i$  factor in Eq. 14).

In the lower panels of Fig. 7 we show the intensity APS, which allow us to estimate the absolute contribution of the different components. Large values of the intensity APS can be obtained from a particularly anisotropic component or from a very bright one. The angular dependence for all components is the same as in the fluctuation APS, but now, due to a very small average intensity, the EG-MSII component has the lowest intensity APS (black solid line), followed by the solid green line, corresponding to the sum of the EG-MSII and EG-UNRESMain components (even if the fluctuation APS is larger for the former than for the latter). Once the full

extragalactic emission is considered (solid red and blue lines), the intensity APS is between a factor of 100 and  $5 \times 10^4$  larger than the intensity APS of EG-MSII, depending on the subhalo boost used. Notice that the solid yellow and purple lines (that only include resolved (sub)halos and the subhalo boost to the resolved main halos) have essentially the same intensity APS as the solid red and blue lines, which implies that the total intensity APS of the DM annihilation signal is dominated by the extragalactic unresolved subhalos of the massive main halos.

In the case of DM decay (right panels), we can see that the fluctuation APS of the EG-MSII component (solid black line) has the same shape as the solid green line (which adds the contribution

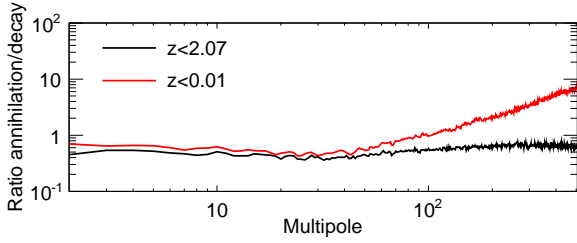


**Figure 8.** Ratio of the fluctuation APS of the extragalactic maps (resolved (sub)halos, EG-MSII) between the case of annihilating and decaying DM (for the same particle physics models as in previous figures). The black line corresponds to the DM-induced emission up to  $z < 2.07$  while the red line only accounts for the emission in the first shell ( $z < 0.01$ ).

of EG-UNRESMain), but a higher normalization. This is because the signal is dominated by the massive resolved (sub)halos. We also see this in the case of the intensity APS (bottom right panel), where the contribution of low-mass halos to the intensity APS is essentially negligible (the solid green line overlaps with the solid black line).

The fluctuation APS of the extragalactic maps for the case of DM annihilation and DM decay are very similar. This can be seen more clearly in Fig. 8, where we plot the ratio of the fluctuation APS of the EG-MSII component in the case of annihilating and decaying DM. The black line corresponds to the APS of the past-light cone up to  $z < 2.07$ , while for the red line we only consider the first concentric shell ( $z < 0.01$ ). The red line shows that the annihilation and decay cases are different mainly at large multipoles ( $\ell > 50 - 60$ ) where the APS is sensitive to the inner halo profile: the more extended the surface brightness profile is, the less steep the APS is. Thus, we expect the APS to be steeper (at large multipoles) for the case of annihilating DM than for decaying DM. However, this effect is only evident for the objects that are closer to us: (sub)halos that are further away appear point-like (for the angular resolution of the maps) and, in that case, the signal from annihilation and decay becomes indistinguishable, as is shown by the black line in Fig. 8.

### 5.2.2 Galactic APS

The dashed lines in Fig. 7 indicate our results for the APS of the galactic components. They can be summarized as follows:

*MW smooth halo:* since the position of the observer is offset with respect to the GC, the DM-induced emission associated with our own galaxy is larger when looking towards the GC. This creates a large scale dipole<sup>15</sup>, that can be seen in the APS of the smooth component (dashed green lines in Fig. 7), which decreases more rapidly for the case of decay than for annihilation since the luminosity profile is more centrally concentrated in the latter.

*Resolved AQ subhalos (GAL-AQ):* in contrast to the previous case, the emission from the resolved subhalos (GAL-AQ, dashed black lines) is much more anisotropic at larger multipoles, being rather similar in shape to the extragalactic one. The exact shape of the GAL-AQ contribution can be affected by the position of the observer relative to the local subhalo population: if a subhalo is very close to the observer, it would appear as a very extended source

<sup>15</sup> Strictly speaking the effect of having an emission peaking towards one particular direction does not affect only the APS at  $\ell = 1$ , as a real dipole, but extends to much larger multipoles.

in the sky map increasing the power at low multipoles, making the APS steeper. In order to quantify this effect, we constructed 100 different sky-maps of the GAL-AQ component, randomly changing the position of the observer in the surface of a sphere centered in the GC with a radius of 8.5 kpc. We find that the first and third quartiles of the distribution (at  $\ell = 200$ ) are located only a factor of 2 below and above the median, respectively.

*Unresolved galactic subhalos (GAL-UNRES):* to evaluate the contribution of unresolved galactic subhalos to the APS we follow the method presented in Ando (2009), which uses analytical relations to calculate the APS from galactic substructures for a specified subhalo distribution and luminosity function. The details of our implementation are described in Appendix D. Basing our subhalo models on the results of Springel et al. (2008) (both for a LOW and HIGH boost), the contribution of unresolved galactic substructures to the intensity APS is small: for annihilation, the contribution to the APS is less than  $\sim 10\%$  of that from resolved subhalos, while for decay their contribution is at most a few percent of that from resolved subhalos. We therefore choose to not include this contribution to the APS.

Overall, considering the galactic and extragalactic contributions, the APS signal is clearly dominated by the smooth halo component in the case of DM annihilation, although the extragalactic emission could be important at very large multipoles ( $\ell \gtrsim 300$ ) if subhalos give a large boost. On the contrary, for DM decay, the extragalactic emission dominates already from  $\ell \gtrsim 20$  and it is only at the very large scales that the anisotropy of the smooth halo dominates the signal. However, if a mask is introduced along the galactic plane (as in Ackermann et al. 2012a), we expect that the balance between galactic and extragalactic components will change, reducing significantly the impact of all the components characterized by a large emission around the GC (see Sec. 6).

## 6 DISCUSSION

### 6.1 Redshift dependence of the extragalactic APS

In Fig. 9, we divide the extragalactic gamma-ray emission in redshift bins (each bin including 4 MS-II snapshots) and compute the fluctuation APS for the EG-LOW component (i.e. the total emission, including all (sub)halos, down to  $M_{\min} = 10^{-6} M_{\odot}/h$  and with a LOW subhalo boost) in each bin. The APS is computed at an energy of 4 GeV. We can see that for both, DM annihilation (left panel) and DM decay (right panel), the lower redshifts are characterized by a larger anisotropy. This is due to the fact that the volume of the past light cone grows with redshift, as well as the number of gamma-ray emitting (sub)halos. Thus, the first snapshots are those characterized by the lowest number of (sub)halos and are more affected by their discrete distribution. Moreover, the clustering of DM (sub)halos is larger at lower redshifts. The peaks that move towards higher multipoles with increasing redshift are a remnant of the spurious effect related to the periodicity of the MS-II box discussed in Sec. 3.1. For a particular redshift, the peaks indicate the angular size of the MS-II box at that redshift (what we called  $\ell^*$  in Sec. 3.1): multipoles smaller than  $\ell^*$  are affected by a loss of power due to the missing modes at wavelengths larger than the MS-II box, and therefore we cannot trust our predictions below  $\ell^*$ . This fact is, however, not relevant for a comparison with the Fermi-LAT APS data, since we are mainly interested in the multipole range between  $\ell = 155$  and 500, where the extragalactic APS is dominated by the first redshifts, for which  $\ell^* < 20 - 30$ .

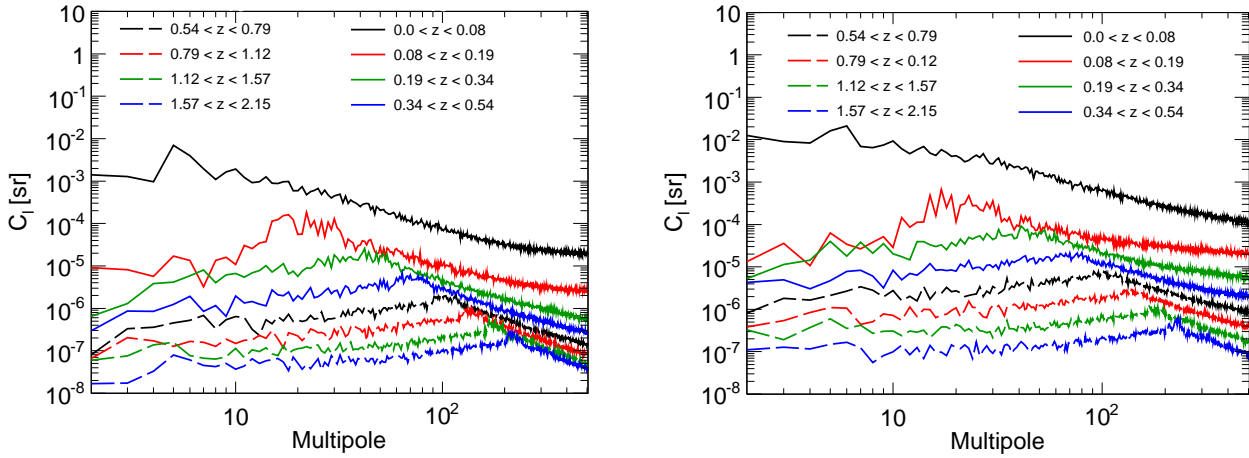


**Figure 9.** Fluctuation APS for the extragalactic gamma-ray intensity coming from DM annihilation (left) and DM decay (right) for different redshift bins. The APS is computed at an energy of 4 GeV and for the LOW subhalo boost (in the case of annihilation) with  $M_{\min} = 10^{-6} M_{\odot}/h$ . The  $b$ -model is assumed.

## 6.2 Energy dependence of the APS

The extragalactic fluctuation APS increases with increasing energy, a fact already pointed out in the past (Ando & Komatsu 2006; Zavala et al. 2010; Ibarra et al. 2010) and related to the redshift dependence discussed in the previous section: following Eq. 14, the total fluctuation APS at a particular energy  $E_{\gamma}$  can be written as the sum  $\sum_i f_i^2(E_{\gamma}) C_i^{\text{fluct}}$  over the fluctuation APS of each concentric shell  $C_i^{\text{fluct}}$  normalized by the square of the relative emission in the  $i$ -th shell with respect to the total. Since individual shells are thin in redshift space, each single  $C_i^{\text{fluct}}$  does not depend on energy, and thus changing the energy only has the effect of modifying the  $f_i$  factors that determine the balance among the APS of the different shells. These  $f_i$  factors depend on the annihilation/decay channel selected for the particular DM candidate, as well as on how much the DM density changes with  $z$  within a particular shell (see Fig. 5). For high energies, the shells that contribute the most to the signal, i.e. those with the largest  $f_i$  factors, are the first shells, which are characterized by the largest APS. Thus, the total fluctuation APS increases as energy increases.

Note, however, that in the cases where the fluctuation APS is dominated by the galactic emission, the fluctuation anisotropy will not change with energy, neither in normalization nor in shape.

## 6.3 Inner density profile of DM (sub)halos

When dealing with the extragalactic emission, we have assumed that (sub)halos have a smooth NFW density profile, which is characterized by a slope that tends asymptotically to  $-1$  for small radii, and lies between the steeper Moore (Moore et al. 1999) and cored Burkert (Burkert 1996) profiles. Current high resolution  $N$ -body simulations have demonstrated that the Einasto profile (Eq. 12) produces an even better fit than NFW. The slope of the Einasto profile decreases as a power-law as the distance from the center decreases, and it is shallower than NFW at small radii.

It is also important to note that the process of galaxy formation within DM halos has an impact on the DM distribution in the central regions where it is believed that the halo is adiabatically contracted resulting in a more concentrated DM distribution (e.g. Mo et al. 1998; Gnedin et al. 2004; Ahn et al. 2007). However, re-

cent hydrodynamical simulations with strong supernovae feedback claim that including the effect of baryons can actually result in the development of a central DM core in intermediate mass halos (Pontzen & Governato 2011; Maccio' et al. 2011).

For the extragalactic emission, the uncertainty on the inner DM density profile has very limited effect on the APS since only a small fraction of (sub)halos cover more than one pixel in our maps, and also because, even if the object is characterized by extended emission, the difference between a cuspy or cored profile is only noticeable at very small projected radii. On the other hand, we do expect a change in the total intensity of the DM-induced emission: for instance, if an Einasto profile is used instead of a NFW, the annihilation rate per halo will increase by 50% (Zavala et al. 2010). Considering the extreme cases of a Burkert and a Moore profile, the difference is roughly an order of magnitude (Profumo & Jeltama 2009). For decaying DM the total luminosity of a halo is directly proportional to its mass, independently of the DM profile assumed.

For the galactic emission, the reasoning above applies to the resolved subhalos. On the other hand, assuming a different profile for the smooth halo may have a stronger impact on the APS, since this represents the largest contribution (at least at low multipoles, and particularly for the case of annihilating DM). The effect of assuming a NFW<sup>16</sup> rather than an Einasto profile is evident at low multipoles (with the APS of the former being smaller than the APS of the latter), but the difference becomes smaller at larger multipoles. This can be explained by noting that the emission towards the GC is larger with respect to the anti-center in the case of an Einasto profile<sup>17</sup>, resulting in a more anisotropic APS. The differences are less evident for the case of decaying DM.

Finally, it is important to remember that any uncertainty in the inner MW density profile will be reduced if the region around the GC is masked. For instance, for  $|b| > 30^\circ$ , the different reasonable DM profiles are practically indistinguishable (Bertone et al. 2009).

<sup>16</sup> Taken from Prada et al. 2004 and normalized to the same local density than the Einasto profile introduced in Sec. 4.1.

<sup>17</sup> If the two profiles are normalized to the same density at 8.5 kpc, the NFW will have a larger intensity within  $\sim 10$  pc, but in the region between  $\sim 1$  kpc and 10 kpc from the GC (where the majority of the emission comes from) an Einasto profile is characterized by a larger density.

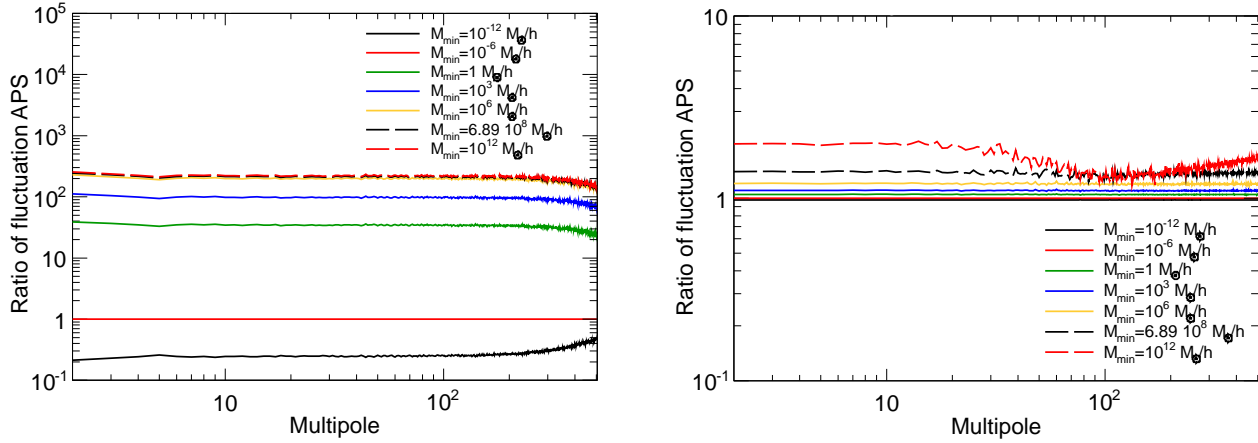


**Figure 11.** Ratio of the total fluctuation APS (galactic and extragalactic) for different values of  $M_{\min}$  with respect to the reference case  $M_{\min} = 10^{-6} M_{\odot}/h$ . The APS is computed at 4 GeV. The left panel refers to the case of annihilating DM with the HIGH subhalo boost, while the right panel is for decaying DM.

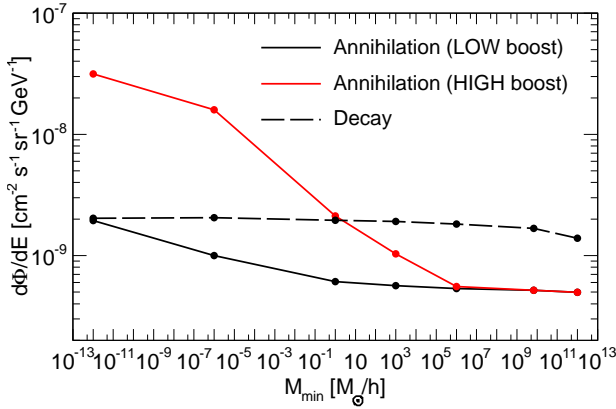


**Figure 10.** Total gamma-ray intensity from DM annihilation (solid lines) and DM decay (dashed lines) at 4 GeV as a function of the minimal halo mass  $M_{\min}$ . The LOW and HIGH subhalo boosts (see Secs. 3.3 and 4.2) are shown with black (red) lines, respectively. The emission has been computed only for the values of  $M_{\min}$  indicated by the full dots, while the lines are obtained by interpolation.

#### 6.4 The minimum self-bound halo mass $M_{\min}$

The particle nature of DM determines the small-scale cutoff in the matter power spectrum of density fluctuations, and hence, the value of  $M_{\min}$ . For neutralinos, the most common WIMP DM candidates, typical values for  $M_{\min}$  go from  $10^{-11} M_{\odot}/h$  to  $10^{-3} M_{\odot}/h$  (e.g. Bringmann 2009). Although this range can be considered as a reference for all WIMP candidates, a particular scenario might lie outside this range. In order to investigate the impact of different values of  $M_{\min}$  in our predictions, we generate template maps for  $M_{\min}$  equal to  $10^{-12} M_{\odot}/h$  and  $1 M_{\odot}/h$ . We also consider a few larger values (namely  $M_{\min} = 10^3, 10^6, 6.89 \times 10^8$  and  $10^{12} M_{\odot}/h$ ) that, although clearly far above the expected mass range for WIMP models, are discussed in order to understand how halos of different masses contribute to the gamma-ray intensity and APS.

In terms of the mean gamma-ray intensity, we can see the impact of changing  $M_{\min}$  in Fig. 10; solid (dashed) lines for the

case of DM annihilation (decay), while black and red lines refer to the LOW and HIGH subhalo boosts, respectively. For annihilation, the mean flux decreases only by a factor of  $\sim 5$  between  $M_{\min} = 10^{-12} M_{\odot}/h$  and  $1 M_{\odot}/h$ , for the LOW case, while the difference is one order of magnitude for the HIGH case. For even higher values of  $M_{\min}$ , the intensity stays essentially constant for the LOW case, while it decreases further for the HIGH case until reaching a plateau. In both cases, the point where the intensity reaches an approximately constant value marks the region where the total intensity passes from being dominated by the extragalactic component (for low  $M_{\min}$ ) to being dominated by the emission in the MW (for larger  $M_{\min}$ ). The transition happens at the larger values of  $M_{\min}$  for the HIGH subhalo boost, because (see Sec. 5.1) increasing the subhalo abundance produces more significant effects for the extragalactic emission than for the galactic one.

In the case of DM decay (as discussed before), the bulk of the emission is dominated by large mass halos and, in particular, is already accounted for in (sub)halos with masses larger than  $10^8 - 10^9 M_{\odot}/h$ , with smaller objects contributing only marginally.

The effect of  $M_{\min}$  on the total APS is shown in Fig. 11: the two panels indicate the ratio of the fluctuation APS at 4 GeV for 7 values of  $M_{\min}$  with respect to the reference case of  $M_{\min} = 10^{-6} M_{\odot}/h$ . The panel on the left shows the case of an annihilating DM candidate with a HIGH subhalo boost: looking at Fig. 7, for  $M_{\min} = 10^{-6} M_{\odot}/h$ , the total intensity APS is dominated by the MW smooth halo, while the contribution of extragalactic (sub)halos plays a role only at large multipoles. Now, going from  $M_{\min} = 10^{-6}$  to  $10^{-12} M_{\odot}/h$  does not have a strong impact on the galactic component but it makes the total extragalactic emission increase by a factor of a few (see Fig. 10). The net effect, following Eq. 14, is that the total fluctuation APS decreases because less intensity is associated with the component that dominates the intensity APS (i.e. the galactic one). This is also the reason why the total fluctuation APS increases from  $M_{\min} = 10^{-6}$  to  $1, 10^3$  and  $10^6 M_{\odot}/h$ . When the total emission starts to be dominated by the MW smooth halo (i.e. above approximately  $\sim 10^6 M_{\odot}/h$ ), there is essentially no change to the APS due to variations in  $M_{\min}$ .

The same features appear in the case of a LOW subhalo boost (the figure is not present), even if this case is characterized by a smaller relative difference (all the lines are within one order of magnitude), and, since the emission of the DM smooth halo starts



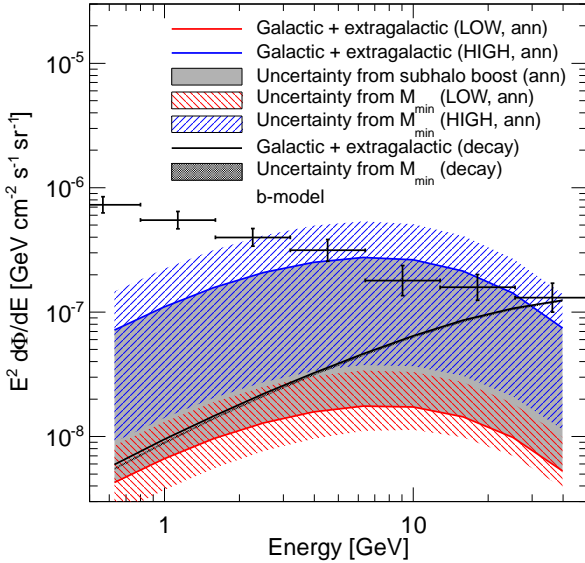


**Figure 12.** Energy spectrum of the average gamma-ray intensity from DM annihilation (color lines) or decay (black line) from extragalactic and galactic (sub)halos. The blue and red lines correspond to the LOW and HIGH subhalo boosts, respectively, so that the filled grey area between them corresponds to the uncertainty due to the subhalo boost, for a fixed value of  $M_{\min}$ . The red (blue) shaded area around the red (blue) solid line indicates the uncertainty in changing the value of  $M_{\min}$  from  $10^{-12}$  to  $1 M_{\odot}/h$ , for the LOW (HIGH) scenario boost. The solid black line shows the prediction for a decaying DM candidate and the black shaded area (appearing as a thickening of the solid black line) indicates the uncertainty in changing  $M_{\min}$  from  $10^{-12}$  to  $1 M_{\odot}/h$ . The observational data points with error bars refer to the measurement of the IGRB as given in Abdo et al. (2010c). Only the emission with  $|b| > 10^\circ$  is considered. The DM candidates are described in Sec. 2.

to dominate already at  $M_{\min} = 1 M_{\odot}/h$ , the APS does not change for  $M_{\min}$  larger than that value.

The right panel in Fig. 11 is for decaying DM: the different lines follow the same behaviour as for annihilating DM but the effect of changing  $M_{\min}$  is highly reduced. The only important deviation is for the largest value of  $M_{\min}$ : at low multipoles the APS is still dominated by the smooth MW halo and, thus, we expect only a different normalization. However, when the extragalactic component becomes relevant, the dashed red line decreases because the extragalactic fluctuation APS for  $M_{\min} = 10^{12} M_{\odot}/h$  is smaller than the case at  $M_{\min} = 10^{-6} M_{\odot}/h$  since it is sensitive, at these multipoles, to the inner DM profile of the largest objects.

### 6.5 Theoretical uncertainty bands

In the current section we summarize our predictions for the energy and angular power spectra of the DM contribution to the IGRB emission. We also present “theoretical error bands” that bracket the uncertainties discussed in the previous sections. These predictions are given only for a fixed particle physics scenario (the *b*-model, see Sec. 2), while the analysis of different DM candidates, (i.e., changing  $m_\chi$ , the annihilation cross section, decay life time and annihilation/decay channels), will be discussed in a follow-up paper.

The energy spectrum of the DM-induced signal (averaged over the region with  $|b| > 10^\circ$ ) is shown in Fig. 12. The grey area be-

tween the red (LOW subhalo boost) and blue line (HIGH subhalo boost) spans approximately a factor of 50 and quantifies the uncertainty associated with the unknown subhalo boost, for a fixed value of  $M_{\min} = 10^{-6} M_{\odot}/h$ . The additional red and blue shaded areas indicate the uncertainties introduced by changing the value of  $M_{\min}$  between  $10^{-12} M_{\odot}/h$  and  $1 M_{\odot}/h$ . For the case of decaying DM, our predictions are completely determined by massive (sub)halos so the theoretical uncertainties are much smaller than for the case of DM annihilation. The Fermi-LAT data from Abdo et al. (2010c) are also plotted with error bars.

Fig. 13 summarizes our predictions for the DM-induced APS (intensity APS in the left panel and fluctuation APS in the right panel). Contrary to the plots presented in the previous sections, the APS is now computed after having integrated the gamma-ray emission between 2 and 5 GeV. Moreover, the APS has been averaged in bins of  $\Delta\ell = 50$  starting from  $\ell = 5$ , and we introduce a mask covering the region with  $|b| < 30^\circ$ . We approximately correct for the effect of the mask by dividing the raw APS by the fraction of the sky  $f_{\text{sky}}$  left unmasked, as it was done in Ackermann et al. (2012a). All of this is for comparison purposes with the Fermi-LAT APS data in the same energy bin, taken from Ackermann et al. 2012a<sup>18</sup>. The inclusion of the mask has strong effects both on the average emission of the smooth MW halo and on its APS since we are masking the region where the signal peaks. On the other hand, it has a limited effect on the extragalactic emission. After masking, the total intensity APS for annihilating DM is dominated by the resolved galactic subhalos in the case of the LOW subhalo boost and by the extragalactic unresolved (sub)halos for the HIGH subhalo boost, i.e., contrary to what is shown in Fig. 7, the smooth MW halo only represent a subdominant contribution. For decaying DM, all these three components (extragalactic emission, resolved galactic subhalos and the smooth MW halo) have a comparable intensity APS.

In Fig. 13, the red and blue lines indicate our predictions for an annihilating DM candidate in the LOW and HIGH scenario, respectively. Thus, the grey area indicates the uncertainty associated with the unknown subhalo boost. If we had plotted only the extragalactic intensity APS in the left panel, the LOW case would have been a factor 500 below the line for the HIGH case (as in Fig. 7). However, the resolved galactic subhalos increase the intensity APS for the LOW case, while having a less important role for the HIGH case. Thus, the red and blue lines are only one order of magnitude away from each other. Moreover, the uncertainty due to  $M_{\min}$  is completely negligible in the LOW case since the APS is determined by the galactic resolved subhalos, and thus is not sensitive to changes in  $M_{\min}$ . The same is true for the case of decaying DM (black line), whose APS is determined by massive (sub)halos.

The right panel of Fig. 13 shows the fluctuation APS: the red line, corresponding to the LOW subhalo boost is now above the blue line, relative to the HIGH subhalo boost. This is because the galactic subhalos (the component that dominates the total APS in the former case) are associated with a larger intrinsic anisotropy than the extragalactic (sub)halos, which dominate the APS in the latter case.

We conclude this section with a comment on the comparison between our predictions for the DM-induced APS with the Fermi-LAT data shown in Fig. 13. Although a rigorous comparison is left for future work we can already see that the fluctuation APS from

<sup>18</sup> We do not mask the point sources in the 1-year catalog, as in Ackermann et al. (2012a), so that our  $f_{\text{sky}}$  is 0.5.



DM annihilation is of the same order, and has a similar shape, as the data (at least in the case of the LOW subhalo boost). On the contrary, for a decaying DM candidate, the predictions are not compatible with a flat APS and they are also characterized by a normalization which is too low.

Nevertheless, even if the annihilating DM candidate we used here is able to reproduce the same level and shape of the fluctuation APS inferred from the data, it still does not represent a viable interpretation, since such a candidate is characterized by a very low intensity APS (left panel). Improvements in the analysis of the gamma-ray data are still possible both from the experimental side (e.g. increasing the statistics, especially at high energies), and from the theoretical side (e.g. one can think of selecting, for each DM candidate, the energy bin that maximizes the DM-induced intensity APS).

## 7 SUMMARY AND CONCLUSIONS

In the present paper we generated all-sky gamma-ray maps from the annihilation/decay of DM in extragalactic (sub)halos and in the halo and subhalos of the MW. Apart from the prompt gamma-ray emission, we also considered emission due to the IC scattering of  $e^+/e^-$  produced in the annihilation or decay with CMB photons and, for the smooth MW halo, additional contributions from starlight (either directly or re-scattered by dust) and the so-called “hadronic emission” (see Appendices A and B) are also considered.

The DM distribution was modeled using state-of-the-art  $N$ -body simulations: Millennium-II for extragalactic (sub)halos and Aquarius (Aq-A-1) for the galactic halo and its subhalos. To compute the extragalactic emission, we improved the algorithm described in Zavala et al. (2010) and simulated the past light cone up to  $z = 2$ . The MS-II allows us to account for the emission of structures with a mass larger than  $M_{\text{res}} \sim 10^9 M_\odot/h$ . We then considered the intensity from unresolved (sub)halos down to a minimum self-bound mass  $M_{\text{min}}$ , by a hybrid method that combines an extrapolation of the behaviour of the least massive resolved halos in MS-II with the subhalo boost model introduced in Kamionkowski & Koushiappas (2008) and Kamionkowski et al. (2010) and refined in Sánchez-Conde et al. (2011). On the other hand, the galactic emission was modeled assuming that the smooth halo of the MW is given by an Einasto profile, renormalized to a value of  $0.3 \text{ GeV/cm}^3$  for the local DM density. Resolved galactic subhalos are taken directly from the Aquarius simulation (down to a mass of  $\approx 10^5 M_\odot$ ), while the contribution of unresolved galactic subhalos is estimated by means of the same procedure used for the extragalactic emission.

The template maps of the DM-induced emission were then used to derive the energy spectrum of the different components from 0.5 GeV and 50 GeV (see Fig. 6). The main goal of the paper is the characterization of the anisotropies of the DM-induced emission, which was done in Sec. 5.2, where we computed the APS of the different components up to  $\ell = 500$  (see Fig. 7), which is the range covered by the recent Fermi-LAT analysis of the APS of the diffuse gamma-ray emission (Ackermann et al. 2012a).

We also discuss the possible effects of modifying some of the assumptions in our modeling of the DM distribution. Most notably, we consider two different scenarios with a small and a large subhalo contribution (referred to as LOW and HIGH throughout the text). Additionally, we study how the energy spectrum and APS depend on the value of the minimal self-bound halo mass  $M_{\text{min}}$ . A discussion on the effects of using different DM halo profiles is also given.

Quantifying the impact of these uncertainties helps us understanding which are the ones that primarily affect the APS, as well as to associate a “theoretical uncertainty band” to our predictions.

The main results of our study are:

- An improvement of the procedure used in Zavala et al. (2010) to compute the extragalactic DM-induced intensity introducing independent rotations for each of the replicas of the simulation box. This notably reduces spurious features in the APS of the simulated maps due to residual correlations introduced by the periodicity of the MS-II box.
- For annihilating DM, the total extragalactic emission (once all (sub)halos down to  $M_{\text{min}} = 10^{-6} M_\odot/h$  are considered) is a factor of 20 (500) larger than the emission produced in the (sub)halos resolved by the MS-II simulation. On the other hand, the extragalactic emission for decaying DM is dominated by the structures resolved in the simulation, with a total intensity that only increases by a factor of 2 once unresolved objects are taken into account.
- The effect of including unresolved subhalos is less important for the galactic component, since these are mainly located in the outskirts of the MW halo, far from the observer, contrary to the nearby GC that produces a significant contribution to the signal. Our prediction for the total galactic intensity (down to  $M_{\text{min}} = 10^{-6} M_\odot/h$ ) is between a factor of 2 and 10 times larger than the emission of the smooth MW (for annihilating DM). The contribution of unresolved subhalos is negligible in the case of DM decay.
- The extragalactic intensity APS in the case of annihilating DM is dominated by unresolved (sub)halos. The intensity APS of the total emission is between 100 and  $5 \times 10^4$  times larger than if only the resolved MS-II (sub)halos are considered, even though its fluctuation APS is lower than the fluctuation APS of the resolved component. In the case of the galactic substructures, the intensity APS is dominated by the resolved subhalos (which have the largest intrinsic anisotropies of all components) in the Aquarius halo (down to  $\sim 10^5 M_\odot$ ), while unresolved subhalos are not expected to contribute. The total intensity APS is dominated by the smooth DM halo of the MW, at least for low multipoles, while above  $\ell = 300$ , the extragalactic contribution becomes important (if the HIGH subhalo boost is assumed).
- The case of decaying DM is quite different: the APS of the smooth MW halo decreases more rapidly, so that the total intensity APS is dominated by extragalactic halos around  $\ell = 20 - 30$ . Galactic subhalos, on the other hand, are characterized by large anisotropies but their low intensity forces them to play only a minor role in the total intensity APS.
- Both for annihilating and decaying DM, the total intensity APS depends mainly on structures in the local Universe, with objects located at  $z > 0.26$  contributing to less than 10% of the total signal.
- Changing the value of  $M_{\text{min}}$  from 1 to  $10^{-12} M_\odot/h$  has a very small effect for decaying DM, while our predictions can change dramatically for annihilating DM, especially for a HIGH subhalo boost: the left panel of Fig. 13 shows that an uncertainty of almost two orders of magnitude is associated with the total intensity APS in this case.

In a future work the DM template maps produced here will be used to derive constraints on the particle physics nature of DM from a comparison with the Fermi-LAT data. In Fig. 13 we made a first comparison for a particular DM candidate used in this work and find that even if the DM-induced fluctuation APS is of the same order of the Fermi-LAT data (for DM annihilation), this particular DM candidate is not able to account for the bulk of the signal de-

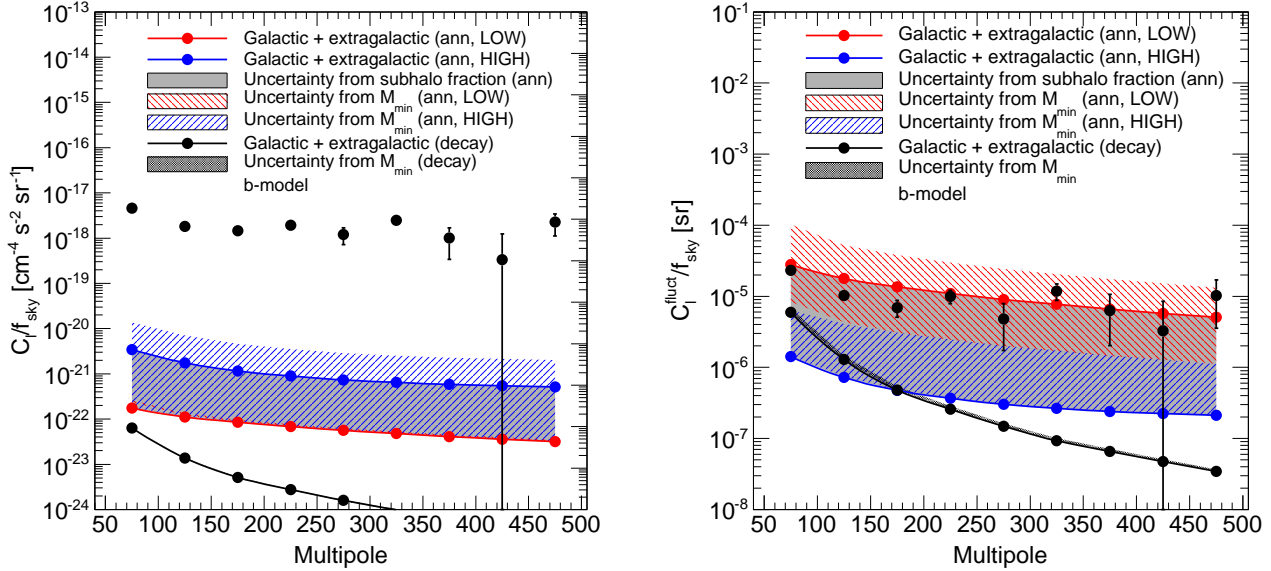


**Figure 13.** Total intensity APS of the gamma-ray emission from DM annihilation (color lines) or decay (black line) in extragalactic and galactic (sub)halos. The blue and red lines correspond to the LOW and HIGH subhalo boosts, respectively, so that the filled grey area between them corresponds to the uncertainty due to the subhalo boost, for a fixed value of  $M_{\min}$ . The red (blue) shaded area around the red (blue) solid line indicates the uncertainty in changing the value of  $M_{\min}$  from  $10^{-12}$  to  $1 M_{\odot}/h$ , for the LOW (HIGH) case. The solid black line shows the prediction for a decaying DM candidate and the small black shaded area, appearing as a thickening of the solid black line, indicating the uncertainty in changing  $M_{\min}$  from  $10^{-12}$  to  $1 M_{\odot}/h$ . The APS is measured in the energy bin between 2 to 5 GeV. The observational data points with error bars refer to the measurement of the APS as given in Ackermann et al. (2012a). A region of  $30^\circ$  around the galactic plane has been masked and the APS has been binned with a binsize of  $\Delta\ell = 50$ . The DM candidates are described in Sec. 2.

ected by Fermi-LAT since its intensity APS is too low. A more rigorous comparison (coupled with a scan over a reasonable set of DM models and using a broader energy range) is still required in order to derive more conclusive statements. Based on the energy spectra of the DM candidates considered here relative to the measured IGRB (see Fig. 6), the APS of the 2-5 GeV energy band shown in Fig. 13 is likely not the optimal choice for setting constraints, but it should be considered as an example for the comparison between the Fermi-LAT data and our predictions.

It is also important to note that the majority of the IGRB emission is expected to be produced by standard astrophysical unresolved sources, such as blazars, star-forming galaxies and pulsars. Thus, a complete study of the IGRB emission can only be performed with a model that also includes these contributions. In this case, the so-called “energy anisotropy spectrum”, i.e. the fluctuation APS at a fixed multipole but as a function of the energy, is a particularly useful observable since it has been shown that modulations in the energy anisotropy spectrum may mark transitions between regimes where different classes of sources are responsible for the bulk of the IGRB intensity (Siegal-Gaskins & Pavlidou 2009).

In any case, the study of the IGRB energy spectrum and of its anisotropies are not the only tools one can resort to for the study of the IGRB nature. For instance, in Xia et al. (2011) the authors compute the cross-correlation of the Fermi-LAT data with the angular distribution of objects detected in different galaxy surveys. Assuming that these objects represent the detected counterparts of unresolved astrophysical sources contributing to the IGRB, they used the cross-correlation measurement to put constraints on the IGRB composition. Moreover, Dodelson et al. (2009), Baxter et al. (2010) and Malyshev & Hogg (2011) showed that the analysis of

the probability distribution of the photon counts can be used efficiently to distinguish a DM signal from a cumulative emission of astrophysical sources in the IGRB data. In principle, the maps produced in the present paper represent unique tools to extend the techniques exploited in Xia et al. (2011) and Dodelson et al. (2009) by including a possible DM contribution.

## ACKNOWLEDGMENTS

We thank Alberto Dominguez for providing us with tables for the EBL attenuation factor. JZ thanks Niayesh Afshordi for fruitful discussions. We thank Alessandro Cuoco and Anne Green for useful comments and discussions. We also thank Chris Hirata and the support of the Consolider-Ingenio 2010 Programme under grant MultiDark CSD2009-00064. JZ is supported by the University of Waterloo and the Perimeter Institute for Theoretical Physics. Research at Perimeter Institute is supported by the Government of Canada through Industry Canada and by the Province of Ontario through the Ministry of Research & Innovation. JZ acknowledges financial support by a CITA National Fellowship. JSG acknowledges support from NASA through Einstein Postdoctoral Fellowship grant PF1-120089 awarded by the Chandra X-ray Center, which is operated by the Smithsonian Astrophysical Observatory for NASA under contract NAS8-03060. TD was supported by the Spanish MICINN Consolider-Ingenio 2010 Programme under grant CPAN CSD2007-00042. We also thank the support of the MICINN under grant FPA2009-08958, the Community of Madrid under grant HEPHACOS S2009/ESP-1473, and the European Union under the Marie Curie-ITN program PITN-GA-2009-237920. The calculations for this paper were performed on the ICC Cosmology Machine, which is part of the DiRAC Facility jointly

funded by STFC, the Large Facilities Capital Fund of BIS, and Durham University, and the clusters at the Max Planck Institute for Astrophysics. We acknowledge use of the facilities of the Shared Hierarchical Academic Research Computing Network (SHARC-NET:www.sharcnet.ca) aCompute/Calcul Canada.

## APPENDIX A: INVERSE COMPTON EMISSION

The secondary IC emission has been described in detail in Blumenthal & Gould (1970), where the authors also provide useful formulae to reproduce their calculation. This process consists in a transfer of momentum from a high energy cosmic ray (CR) electron or positron to a low energy photon of the ISRF.

A model for the ISRF provided by Moskalenko et al. (2006) is publicly available on the GALPROP webpage<sup>19</sup>. In order to compute the IC emission using semi-analytical methods, it is convenient to fit the GALPROP model of the ISRF as a sum of five black-body spectra (e.g. Delahaye et al. 2010). One of these is the CMB, while the others come from a fit to the model and have less physical meaning, although they derive from dust and stellar emissions. In this procedure, it is necessary to assume a homogeneous ISRF which might impact on the morphology of the resulting gamma-ray emission, although it should be quite moderate since variations of the ISRF affect both the  $e^+/e^-$  spatial density and gamma-ray emissivity in opposite directions.

Apart from the ISRF, one also needs to know the  $e^+/e^-$  distribution and propagation in the galaxy in order to compute the IC emission. These processes are governed by the following diffusion-loss equation (neglecting convection and re-acceleration effects):

$$-\nabla \cdot (D(E, \mathbf{x}) \nabla f) - \frac{\partial}{\partial E} (b(E) f) = Q(E, \mathbf{x}), \quad (\text{A1})$$

where  $f(E, \mathbf{x})$  is the  $e^+/e^-$  number density per unit of energy at the point  $\mathbf{x}$ ,  $D(E, \mathbf{x})$  is the diffusion coefficient while  $b(E)$  describes the energy losses (due to synchrotron and IC emissions). Finally  $Q(E, \mathbf{x})$  indicates the source term which in our case is DM annihilation/decay.

Eq. A1 governs diffusion inside a so-called diffusion zone, outside of which electrons and positrons are not confined by magnetic fields and escape from the galaxy. The coefficients defining the different terms in Eq. A1 are constrained by the available observational data (mainly the boron-to-carbon CR ratio), but important uncertainties are still present (see, e.g. Donato et al. 2004 and their definition of the MIN/MED/MAX scenarios). We use here the semi-analytical methods described in Delahaye et al. (2008) which take into account the full expression of the energy losses in the Klein-Nishina regime.

As explained in Boehm et al. (2010), the morphology of the galactic IC emission created by the  $e^+/e^-$  produced by DM annihilation/decay is very sensitive to the choice of the CR propagation parameters and hence, the results should be taken with caution. Here we use the same propagation model parameters as for the protons and anti-protons related to the hadronic emission (see Appendix B) and we assume the MED scenario mentioned above. The uncertainty in the resulting gamma-ray intensity can be quite large, depending on the arrival direction, and the results can also change with different  $e^+/e^-$  propagation models. Nevertheless, we neglect this source of uncertainty noting that IC emission is relevant only for a fraction of the energy range considered here and

only for massive DM candidates (see Fig. 1): in the case of the  $b$ -model, with a mass of 200 GeV, the IC emission is located almost 2 orders of magnitude below the prompt emission and is dominated by interactions with the ultraviolet component of the ISRF. In the case of a decaying DM particle, though the mass is higher, the signal gets stronger because it is not concentrated around the GC and the average over the whole sky is larger. Moreover, for the case of decaying DM, the signal is proportional to the inverse of the DM mass, whereas in the annihilating case it is inversely proportional to its square. For the  $\tau$ -model the same difference appears between annihilation and decay and it is even stronger since the masses are the same for both cases. Moreover, since in this case the prompt emission is much lower than for the  $b$ -model, IC and prompt emission become of comparable importance, especially below 10 GeV.

The DM-induced IC emission is implemented in a different way for the different components that constitute the emission: for the smooth halo of the MW, the complete ISRF given by Moskalenko et al. (2006) is used, solving Eq. A1 and considering the propagation of  $e^+/e^-$  produced by DM annihilation/decay before they interact with the ISRF. On the other hand, for the extragalactic (sub)halos and for the galactic subhalos (both resolved and unresolved), we only consider IC scattering with the CMB photons, and ignore the propagation of  $e^+/e^-$  (spatial diffusion is ignored in Eq. A1, and only IC energy losses are considered). In principle, the secondary IC emission from massive halos (and some of the most massive subhalos) may be more realistically described if a full propagation model that includes the effect of baryons and secondary emission contributed by starlight and infrared light is applied instead (e.g., see Colafrancesco et al. 2006, 2007 for the case of the Coma galaxy cluster and the Draco dwarf spheroidal). However, the contribution of extragalactic structures and galactic subhalos is dominated by low-mass objects where star formation is highly suppressed and thus are expected to have a rather small stellar component or be devoid of stars.

Finally, we note that when we use the complete ISRF provided in Moskalenko et al. (2006), the template maps for the IC emission (Cartesian maps with  $90 \times 180$  pixels) have a poorer resolution than the maps obtained from the prompt emission (HEALPix Maps with  $N_{\text{side}}=512$ ) due to the substantial numerical effort required in solving Eq. A1. For our purposes it is enough to re-bin the Cartesian maps into a HEALPix pixelization.

## APPENDIX B: HADRONIC EMISSION

The hadronic emission is the mechanism that contributes the least to our signal but it has a different spatial morphology with respect to the others considered in this work. We only account for it in the case of the smooth MW halo. It comes from the interaction of CR protons and anti-protons with interstellar gas. To compute such a component one needs to derive the  $p/\bar{p}$  intensity everywhere in the diffusion halo. To do so, we follow the semi-analytical method of Barrau et al. (2002) using the propagation parameters of the MED scenario in Donato et al. (2004) which gives a good fit to the boron-to-carbon observational data. Once the  $p/\bar{p}$  distribution has been obtained, it is convolved with the gamma-ray production cross section<sup>20</sup> (taken from Huang et al. 2007) and the interstellar gas distribution (taken from Pohl et al. 2008). See Delahaye et al. (2011) for more details on the computation.

<sup>19</sup> <http://galprop.stanford.edu/>

<sup>20</sup> Note that, following F.W. 1967, we consider here that protons and anti-protons have the same cross-section.

Contrary to the IC emission, this component is less dependent on the choice of propagation parameters due to the fact that protons propagate much further than electrons and tend to smooth out all small scale effects. Moreover, the hadronic emission naturally follows the interstellar gas distribution. A source of uncertainty, which we neglect, may come from the presence of DM substructures near the galactic disk, which may alter locally the gamma-ray intensity.

We note that the angular resolution of the hadronic component is mainly limited by the resolution of the gas maps:  $0.5 \text{ deg} \times 0.5 \text{ deg}$  Cartesian maps. As for the case of the IC emission, these maps are transformed into HEALPix maps.

### APPENDIX C: MAP MAKING FOR A GENERIC PARTICLE PHYSICS MODEL

In this section we describe the implementation of an approximate method that can be used to obtain a full-sky map of the DM-induced extragalactic emission for any particle physics model, given a reference map obtained for a specific model. Thanks to this method we only need to run once our map-making code, saving computation time.

For the purposes of computing the DM-induced emission, each particle physics model is defined by the mass of the DM candidate, its annihilation cross section ( $\sigma_{\text{ann}} v$ ) (or decay lifetime  $\tau$ ), and the branching fractions for different annihilation (or decay) channels with the corresponding photon yields,  $B_i$  and  $dN_i/dE$ . Unless the model has a velocity-dependent cross section (a case we do not explore here), ( $\sigma_{\text{ann}} v$ ) is constant, as it is  $\tau$  in the case of decay, and, therefore, it is just a multiplicative factor in Eqs. 1 and 2. The photon yield, however, depends on redshift. In the case of the galactic halo emission, the redshift variation across the DM sources is negligible, but for the extragalactic component, the additional integration over redshift links together the astrophysical and the particle physics factors in Eqs. 1 and 2.

We benefit from the fact that the past-light cone in our simulated maps is divided in concentric shells with a small redshift width  $\Delta z$  (see Sec. 3.1). It is then always possible to find a particular redshift value contained within  $\Delta z$  (called  $z_{\text{ref}}$ ) so that we can take the factor  $dN_\gamma/dE$  outside the integral in Eq. 1 and write the intensity coming from that shell as<sup>21</sup>:

$$\frac{d\Phi}{dE}(E_\gamma, \Psi, \Delta z) = \frac{(\sigma_{\text{ann}} v)}{8\pi m_\chi^2} \sum_i B_i \frac{dN_\gamma^i(E_\gamma(1+z_{\text{ref}}))}{dE} \times \int_{\Delta z} d\lambda(z) \rho^2(\lambda(z), \Psi) e^{-\tau_{\text{EBL}}(z, E_\gamma)}. \quad (\text{C1})$$

In principle, each line of sight (pixel) in the sky map will have a different value of  $z_{\text{ref}}$  (for the same shell) since the integrand in the r.h.s. of Eq. C1 changes according to the DM density field in each direction. The set of values  $\{z_{\text{ref}}^i\}$  corresponding to the pixels in a given map and their average  $\bar{z}_{\text{ref}}$  can be determined by comparing, pixel per pixel, a full map of the DM-induced intensity (using fully Eq. 1) and a map containing only the result of the integral in the r.h.s. of Eq. C1 (which we call a *J*-map). This needs to be done separately for all the different shells since  $z_{\text{ref}}$  changes shell by shell, and then combined to produce the total observed emission map.

There are no approximations made up to this point. We argue now that a map for a generic particle physics model can be

reconstructed multiplying the *J*-map by the corresponding particle physics factor evaluated at the set of  $\{z_{\text{ref}}^i\}$  obtained for our reference case as described above. Moreover, to a very good approximation, the pixel average value  $\bar{z}_{\text{ref}}$  can be used instead of the full set  $\{z_{\text{ref}}^i\}$ . We test these arguments by using this technique to reconstruct the gamma-ray map for an annihilating DM candidate with a mass of 2 TeV, a cross-section of  $(\sigma_{\text{ann}} v) = 3 \times 10^{-26} \text{ cm}^3 \text{ s}^{-1}$  and annihilating only into  $\tau$  leptons obtained from a sky map for a reference case of a DM candidate with a mass of 200 GeV, the same cross section, but with an annihilation channel into bottom quarks. We then compare the reconstructed map with one corresponding to the same particle physics scenario but obtained directly from the complete map-making code. The test is restricted to the EG-MSII component for an energy of 10 GeV and to the simulation output corresponding to  $z = 3.1$  and  $\Delta z = 0.25$ , which is larger than the shell with the largest redshift “thickness” we consider in this work. We find that the reconstructed map has essentially the same APS as the original maps, and the average intensities of the two maps agree at the level of 1%. This reconstruction method is not only precise when the reconstructed map is obtained accounting for the pixel dependence of  $z_{\text{ref}}$ , but also when the constant average value  $\bar{z}_{\text{ref}}$  is used for all pixels.

We are then confident that this procedure can be used to reconstruct maps of the extragalactic gamma-ray emission for any particle physics model.

### APPENDIX D: ANISOTROPY FROM UNRESOLVED GALACTIC SUBHALOS

In the present section we described how we implement the method described in Ando (2009) to compute the APS of galactic unresolved subhalos.

For the subhalo radial distribution we adopt an Einasto profile with parameters chosen to match those of the Aq-A-1 main halo:  $M_{200} = 9.4 \times 10^{11} M_\odot$ ,  $r_{-2} = 199 \text{ kpc}$ ,  $c_{-2} = 1.24$ , and  $\alpha = 0.678$ , with the normalization set by the fraction of the smooth halo mass  $M_{200}$  in subhalos  $f_{\text{sub}}$ . We require  $f_{\text{sub}} = 0.136$  for subhalo masses in the range  $1.7 \times 10^5$  to  $10^{10} M_\odot$ , which is the fraction of the halo mass found in resolved subhalos in Aq-A-1; extrapolating the mass function to  $M_{\text{min}}$  below the minimum resolved subhalo mass leads to larger values of  $f_{\text{sub}}$ . We take the subhalo mass function slope to be  $-1.9$ , and evaluate the anisotropy for several values of  $M_{\text{min}}$ .

The substructure luminosity function for annihilation is determined by assuming the subhalo luminosity is related to the subhalo mass by  $L(M_{\text{sub}}) = AK(M_{\text{sub}}/M_\odot)^\beta$ , with  $K = b_{\text{sh}}(\sigma v)N_\gamma/(2m_\chi^2)$  and  $A$  a normalization set related to the “astrophysical factor”. We consider two sets of the mass-luminosity parameters ( $A$  and  $\beta$ ), chosen to reproduce the LOW and HIGH cases in the text. The HIGH case extrapolates  $L(M_{\text{sub}})$  to  $M_{\text{min}}$  using the same relation found to fit the resolved subhalos in Aq-A-1; the mass-luminosity relation is calibrated to the measured mass-concentration relation and assumes each subhalo is well-described by a NFW density profile. For the HIGH case we take  $A = 6.48 \times 10^9 M_{\text{sub}}^{\text{sub}} \text{ kpc}^{-3}$  and  $\beta = 0.77$ . The LOW case assumes  $A = 3.21 \times 10^8 M_{\text{sub}}^{\text{sub}} \text{ kpc}^{-3}$  and  $\beta = 0.86$  for subhalos with  $M_{\text{sub}} < 1.7 \times 10^5 M_\odot$ , and the same parameters as the HIGH case for subhalos with  $M_{\text{sub}} > 1.7 \times 10^5 M_\odot$ . The LOW case corresponds to a scenario in which subhalo concentrations increase more mildly with decreasing subhalo mass, and hence in the LOW case the contribution to the intensity and APS from low-mass subhalos is reduced relative to the HIGH case. For decay, the subhalo luminosity is always directly proportional to the subhalo mass.

<sup>21</sup> An analogous equation for the case of decaying DM can be written, of course.

We calculated the APS from unresolved subhalos after masking the region with  $|b| < 30^\circ$ . We find that for this subhalo model, the contribution to the total intensity APS from unresolved subhalos for both annihilation and decay is small. For annihilation this contribution is  $\sim 10\%$  of the contribution from the resolved subhalos for the HIGH case, and  $\sim 5\%$  for the LOW case. For both the LOW and HIGH cases the majority of this contribution from unresolved subhalos originates from subhalos with masses above  $\sim 10^3 M_\odot$ . For decay we find that the contribution from unresolved subhalos is at most a few percent of the resolved subhalo anisotropy. Since these contributions are small compared to other sources of uncertainty in the APS, we do not include them.

## REFERENCES

- Abazajian K. N., Blanchet S., Harding J. P., 2011, *Phys.Rev.*, D84, 103007
- Abdo A., et al., 2010a, *JCAP*, 1004, 014
- Abdo A., et al., 2010b, *Astrophys.J.*, 720, 435
- Abdo A., et al., 2010c, *Phys.Rev.Lett.*, 104, 101101
- Ackermann M., et al., 2011
- Ackermann M., et al., 2012a
- Ackermann M., et al., 2012b
- Afshordi N., Mohayaee R., Bertschinger E., 2010, *Phys.Rev.*, D81, 101301
- Ahn E.-J., Bertone G., Merritt D., 2007, *Phys.Rev.*, D76, 023517
- Ajello M., 2011, On the cosmic downsizing of Fermi's FSRQs and on the Isotropic Gamma-Ray Background
- Ando S., 2005, *Phys.Rev.Lett.*, 94, 171303
- Ando S., 2009, *Phys.Rev.*, D80, 023520
- Ando S., Komatsu E., 2006, *Phys.Rev.*, D73, 023521
- Ando S., Komatsu E., Narumoto T., Totani T., 2007a, *Mon.Not.Roy.Astron.Soc.*, 376, 1635
- Ando S., Komatsu E., Narumoto T., Totani T., 2007b, *Phys.Rev.*, D75, 063519
- Ando S., Pavlidou V., 2009, *Mon.Not.Roy.Astron.Soc.*, 400, 2122
- Angulo R., Lacey C., Baugh C., Frenk C., 2008
- Angulo R., White S., 2009
- Arvanitaki A., Dimopoulos S., Dubovsky S., Graham P. W., Harnik R., et al., 2009, *Phys.Rev.*, D79, 105022
- Bardeen J. M., Bond J., Kaiser N., Szalay A., 1986, *Astrophys.J.*, 304, 15
- Barrau A., Boudoul G., Donato F., Maurin D., Salati P., et al., 2002, *Astron.Astrophys.*, 388, 676
- Baxter E. J., Dodelson S., Koushiappas S. M., Strigari L. E., 2010, *Phys.Rev.*, D82, 123511
- Bergstrom L., Bringmann T., Eriksson M., Gustafsson M., 2005, *Phys.Rev.Lett.*, 94, 131301
- Bertone G., Cirelli M., Strumia A., Taoso M., 2009, *JCAP*, 0903, 009
- Bertone G., Hooper D., Silk J., 2005, *Phys.Rept.*, 405, 279
- Bertone G., Zentner A. R., Silk J., 2005, *Phys.Rev.*, D72, 103517
- Bhattacharya D., Sreekumar P., Mukherjee R., 2009, *Res.Astron.Astrophys.*, 9, 1205
- Blumenthal G., Gould R., 1970, *Rev.Mod.Phys.*, 42, 237
- Boehm C., Delahaye T., Silk J., 2010, *Phys.Rev.Lett.*, 105, 221301
- Bolz M., Brandenburg A., Buchmuller W., 2001, *Nucl.Phys.*, B606, 518
- Boylan-Kolchin M., Springel V., White S. D., Jenkins A., 2010, *Mon.Not.Roy.Astron.Soc.*, 406, 896
- Boylan-Kolchin M., Springel V., White S. D., Jenkins A., Lemson G., 2009, *Mon.Not.Roy.Astron.Soc.*, 398, 1150
- Bringmann T., 2009, *New J.Phys.*, 11, 105027
- Bringmann T., Bergstrom L., Edsjo J., 2008, *JHEP*, 0801, 049
- Bringmann T., Doro M., Fornasa M., 2009, *JCAP*, 0901, 016
- Bringmann T., Huang X., Ibarra A., Vogl S., Weniger C., 2012
- Burkert A., 1996, *IAU Symp.*, 171, 175
- Calore F., De Romeri V., Donato F., 2012, *Phys.Rev.*, D85, 023004
- Casanova S., Dingus B., Zhang B., 2008, *AIP Conf.Proc.*, 1000, 40
- Catena R., Ullio P., 2010, *JCAP*, 1008, 004
- Chakraborty N., Fields B. D., 2012
- Choi K.-Y., Lopez-Fogliani D. E., Munoz C., de Austri R. R., 2010, *JCAP*, 1003, 028
- Cholis I., Tavakoli M., Evoli C., Maccione L., Ullio P., 2011
- Cirelli M., Corcella G., Hektor A., Hutsi G., Kadastik M., et al., 2011, *JCAP*, 1103, 051
- Colafrancesco S., Profumo S., Ullio P., 2006, *Astron.Astrophys.*, 455, 21
- Colafrancesco S., Profumo S., Ullio P., 2007, *Phys.Rev.*, D75, 023513
- Cuesta A., Jeltema T., Zandanel F., Profumo S., Prada F., et al., 2011, *Astrophys.J.*, 726, L6
- Cuoco A., Brandbyge J., Hannestad S., Haugboelle T., Miele G., 2008, *Phys.Rev.*, D77, 123518
- Cuoco A., Hannestad S., Haugbolle T., Miele G., Serpico P., et al., 2007, *JCAP*, 0704, 013
- Cuoco A., Komatsu E., Siegal-Gaskins J., 2012
- Cuoco A., Sellerholm A., Conrad J., Hannestad S., 2011, *Mon.Not.Roy.Astron.Soc.*, 414, 2040
- Davis M., Efstathiou G., Frenk C. S., White S. D., 1985, *Astrophys.J.*, 292, 371
- Delahaye T., Fiascon A., Pohl M., Salati P., 2011, *Astron.Astrophys.*, 531, A37
- Delahaye T., Lavalley J., Lineros R., Donato F., Fornengo N., 2010, *Astron.Astrophys.*, 524, A51
- Delahaye T., Lineros R., Donato F., Fornengo N., Salati P., 2008, *Phys.Rev.*, D77, 063527
- Dermer C. D., 2007, *AIP Conf.Proc.*, 921, 122
- Diemand J., Kuhlen M., Madau P., 2006, *Astrophys.J.*, 649, 1
- Diemand J., Kuhlen M., Madau P., Zemp M., Moore B., et al., 2008, *Nature*, 454, 735
- Diemand J., Moore B., Stadel J., Kazantzidis S., 2004, *Mon.Not.Roy.Astron.Soc.*, 348, 977
- Dodelson S., Belikov A. V., Hooper D., Serpico P., 2009, *Phys.Rev.*, D80, 083504
- Dominguez A., Primack J., Rosario D., Prada F., Gilmore R., et al., 2010
- Donato F., Fornengo N., Maurin D., Salati P., 2004, *Phys.Rev.*, D69, 063501
- Dugger L., Jeltema T. E., Profumo S., 2010, *JCAP*, 1012, 015
- Eke V. R., Navarro J., Steinmetz M., 2001, *Astrophys.J.*, 554, 114
- Faucher-Giguere C.-A., Loeb A., 2010, *JCAP*, 1001, 005
- Fields B. D., Pavlidou V., Prodanovic T., 2010, *Astrophys.J.*, 722, L199
- Fornasa M., Pieri L., Bertone G., Branchini E., 2009, *Phys.Rev.*, D80, 023518
- Fornengo N., Pieri L., Scopel S., 2004, *Phys.Rev.*, D70, 103529
- F.W. S., 1967, *SAO Special Report*, 261
- Gabici S., Blasi P., 2003, *Astropart.Phys.*, 19, 679



- Gao L., Frenk C., Jenkins A., Springel V., White S., 2011, *Mon.Not.Roy.Astron.Soc.*, 419, 1721
- Gnedin O. Y., Kravtsov A. V., Klypin A. A., Nagai D., 2004, *Astrophys.J.*, 616, 16
- Gomez-Vargas G., Fornasa M., Zandanel F., Cuesta A., Munoz C., et al., 2012, *JCAP*, 001
- Gorski K., Hivon E., Banday A., Wandelt B., Hansen F., et al., 2005, *Astrophys.J.*, 622, 759
- Huang C.-Y., Park S.-E., Pohl M., Daniels C., 2007, *Astrophys.J.*, 27, 429
- Huang X., Vertongen G., Weniger C., 2011
- Hutsi G., Hektor A., Raidal M., 2010, *JCAP*, 1007, 008
- Ibarra A., Tran D., Weniger C., 2010, *Phys.Rev.*, D81, 023529
- Inoue Y., Totani T., 2009, *Astrophys.J.*, 702, 523
- Iocco F., Pato M., Bertone G., Jetzer P., 2011, *JCAP*, 1111, 029
- Jarosik N., Bennett C., Dunkley J., Gold B., Greason M., et al., 2011, *Astrophys.J.Suppl.*, 192, 14
- Kalashev O. E., Semikoz D. V., Sigl G., 2009, *Phys.Rev.*, D79, 063005
- Kamionkowski M., Koushiappas S. M., 2008, *Phys.Rev.*, D77, 103509
- Kamionkowski M., Koushiappas S. M., Kuhlen M., 2010, *Phys.Rev.*, D81, 043532
- Kolb E., Turner M., 1994, *The early Universe*. Perseus publishing
- Lacki B. C., Horiuchi S., Beacom J. F., 2012
- Lien A., Fields B. D., 2012
- Loeb A., Waxman E., 2000, *Nature*, 405, 156
- Maccio' A. V., Stinson G., Brook C. B., Wadsley J., Couchman H., et al., 2011
- Makiya R., Totani T., Kobayashi M., 2011, *Astrophys.J.*, 728, 158
- Malyshev D., Hogg D. W., 2011, *Astrophys.J.*, 738, 181
- Martinez G. D., Bullock J. S., Kaplinghat M., Strigari L. E., Trotta R., 2009, *JCAP*, 0906, 014
- Massaro F., Ajello M., 2011
- Meade P., Papucci M., Strumia A., Volansky T., 2010, *Nucl.Phys.*, B831, 178
- Mo H., Mao S., White S. D., 1998, *Mon.Not.Roy.Astron.Soc.*, 295, 319
- Moore B., Quinn T. R., Governato F., Stadel J., Lake G., 1999, *Mon.Not.Roy.Astron.Soc.*, 310, 1147
- Moskalenko I. V., Porter T. A., 2009, *Astrophys.J.*, 692, 54
- Moskalenko I. V., Porter T. A., Strong A. W., 2006, *Astrophys.J.*, 640, L155
- Muecke A., Pohl M., 1998
- Narumoto T., Totani T., 2006, *Astrophys.J.*, 643, 81
- Navarro J. F., Frenk C. S., White S. D., 1997, *Astrophys.J.*, 490, 493
- Navarro J. F., Ludlow A., Springel V., Wang J., Vogelsberger M., et al., 2008
- Pato M., Agertz O., Bertone G., Moore B., Teyssier R., 2010, *Phys.Rev.*, D82, 023531
- Pavlidou V., Venters T. M., 2008, *Astrophys.J.*, 673, 114
- Pieri L., Lavalie J., Bertone G., Branchini E., 2011, *Phys.Rev.*, D83, 023518
- Pinzke A., Pfrommer C., Bergstrom L., 2011, *Phys.Rev.*, D84
- Pohl M., Englmaier P., Bissantz N., 2008, *Astrophys.J.*, 677, 283
- Pontzen A., Governato F., 2011
- Prada F., Klypin A., Flix Molina J., Martinez M., Simonneau E., 2004, *Phys.Rev.Lett.*, 93, 241301
- Profumo S., Jeltama T. E., 2009, *JCAP*, 0907, 020
- Profumo S., Sigurdson K., Kamionkowski M., 2006, *Phys.Rev.Lett.*, 97, 031301
- Salucci P., Nesti F., Gentile G., Martins C., 2010, *Astron.Astrophys.*, 523, A83
- Sánchez-Conde M. A., Betancort-Rijo J., Prada F., 2007, *Mon.Not.Roy.Astron.Soc.*, 378, 339
- Sánchez-Conde M. A., Cannoni M., Zandanel F., Gomez M. E., Prada F., 2011, *JCAP*, 1112, 011
- Sheth R. K., Mo H., Tormen G., 2001, *Mon.Not.Roy.Astron.Soc.*, 323, 1
- Siegal-Gaskins J. M., 2008, *JCAP*, 0810, 040
- Siegal-Gaskins J. M., Pavlidou V., 2009, *Phys.Rev.Lett.*, 102, 241301
- Siegal-Gaskins J. M., Reesman R., Pavlidou V., Profumo S., Walker T. P., 2011, *Mon.Not.Roy.Astron.Soc.*, 415, 1074S
- Singal J., Petrosian V., Ajello M., 2012, *Astrophys.J.*, 753, 45
- Springel V., Wang J., Vogelsberger M., Ludlow A., Jenkins A., et al., 2008, *Mon.Not.Roy.Astron.Soc.*, 391, 1685
- Springel V., White S. D., Frenk C. S., Navarro J. F., Jenkins A., et al., 2008
- Springel V., White S. D., Tormen G., Kauffmann G., 2001, *Mon.Not.Roy.Astron.Soc.*, 328, 726
- Stawarz L., Kneiske T., Kataoka J., 2006, *Astrophys.J.*, 637, 693
- Stecker F., Salamon M., 1996, *Astrophys.J.*, 464, 600
- Stecker F., Salamon M., Malkan M., 1993, *Astrophys.J.*, 410, L71
- Stecker F. W., Venters T. M., 2011, *Astrophys.J.*, 736, 40
- Taoso M., Ando S., Bertone G., Profumo S., 2009, *Phys.Rev.*, D79, 043521
- Taylor J. E., Silk J., 2003, *Mon.Not.Roy.Astron.Soc.*, 339, 505
- Ullio P., Bergstrom L., Edsjo J., Lacey C. G., 2002, *Phys.Rev.*, D66, 123502
- Vertongen G., Weniger C., 2011, *JCAP*, 1105, 027
- Vladimirov A. E., Digel S. W., Johannesson G., Michelson P. F., Moskalenko I. V., et al., 2011, *Comput.Phys.Comm.*, 182, 1156
- Vogelsberger M., White S. D., 2010
- Vogelsberger M., White S. D., Helmi A., Springel V., 2007, *Mon.Not.Roy.Astron.Soc.*
- Vogelsberger M., White S. D., Mohayaee R., Springel V., 2009
- White S. D., Vogelsberger M., 2008
- Xia J.-Q., Cuoco A., Branchini E., Fornasa M., Viel M., 2011, *Mon.Not.Roy.Astron.Soc.*, 416, 2247
- Zavala J., Springel V., Boylan-Kolchin M., 2010, *Mon.Not.Roy.Astron.Soc.*, 405, 593
- Zavala J., Vogelsberger M., Slatyer T. R., Loeb A., Springel V., 2011, *Phys.Rev.*, D83, 123513
- Zhao D., Jing Y., Mo H., Boerner G., 2009, *Astrophys.J.*, 707, 354